Applied Ocean Research 154 (2025) 104375

Contents lists available at ScienceDirect

Applied Ocean Research

journal homepage: www.elsevier.com/locate/apor

Optimization of ANN using metaheuristic algorithms for predicting failure envelope of ring foundations on anisotropic clay

Duy Tan Tran [a], Jim Shiau [b], Divesh Ranjan Kumar [c], Van Qui Lai [d,e], Suraparb Keawsawasvong [a,*]

[a] Research Unit in Sciences and Innovative Technologies for Civil Engineering Infrastructures, Department of Civil Engineering, Faculty of Engineering, Thammasat School of Engineering, Thammasat University, Pathumthani, Thailand
[b] School of Engineering, University of Southern Queensland, Toowoomba, 4350, QLD, Australia
[c] Department of Civil Engineering, Faculty of Engineering, Thammasat School of Engineering, Thammasat University, Pathumthani, Thailand
[d] Faculty of Civil Engineering, Ho Chi Minh City University of Technology (HCMUT), 268 Ly Thuong Kiet Street, District 10, Ho Chi Minh City, Vietnam
[e] Vietnam National University Ho Chi Minh City (VNU-HCM), Linh Trung Ward, Thu Duc District, Ho Chi Minh City, Vietnam

ARTICLE INFO

Keywords:
Failure envelope
Ring footing
Anisotropic
Machine learning

ABSTRACT

This paper is concerned with the assessment of *V-H-M* failure envelopes of ring foundations subjected to general loadings on anisotropic clay using adaptive three-dimensional finite element limit analysis (3D AFELA). The 3D analysis involves calculations of the bearing capacity of ring surface foundations for individual vertical force (*V*), horizontal force (*H*), and moment (*M*) using the well-known anisotropic undrained shear (AUS) failure criterion to study the effect of clay anisotropy. Accordingly, the combinations of *V-H, V-M*, and *H-M* load spaces are examined with the use of normalized output parameters ($V/s_{uTC}A$, $H/s_{uTC}A$, and $M/s_{uTC}AB$) and two dimensionless input parameters, including the radius coefficient (r_i/r_o) and the anisotropic factor (r_e). Furthermore, the various characteristics of the failure mechanisms are examined. The study continues with artificial neural network (ANN) models, aiming to evaluate the correlation between input parameters and their corresponding outcomes. Three optimization methods based on metaheuristic algorithms are considered: artificial bee colony (ABC), imperialist competitive algorithm (ICA), and artificial lion optimization (ALO). The ANN-ICA model stands out for its exceptional predictive precision, robustness, and top-ranking efficiency in score analysis. The outcome of the study proves to be both effective and efficient for evaluating the 3D failure envelope of ring foundations on anisotropic clay subjected to combined loadings (*V-H-M*).

1. Introduction

Ring foundations are often used to uphold axisymmetric structures offshore in the middle of the ocean. They are also used for onshore applications, such as cooling towers, storage tanks, radar stations, transmission towers, chimneys, silos, jacket foundations, and bridge piers (Chen et al., 2021; DNV, 1992). Compared with solid circular footings, ring footings notably require less construction material. Fig. 1 presents a schematic of the ring footing used to support a wind turbine structure on the ocean floor.

Early investigations into the behavior of ring foundations under individual static loads were conducted through experimental tests by several researchers, such as Saha (1978), Hataf and Razavi (2003), Boushehrian and Hataf (2003), and El Sawwaf and Nazir (2012). Other analytical studies, such as Kumar and Ghosh (2005), Zhao and Wang (2008), Remadna et al. (2017), and Kumar and Chakraborty (2015), utilized the method of characteristics, whereas numerical studies were carried out by Nayyeri et al. (2016) and Keshavarz and Kumar (2017). Benmebarek et al. (2012), Lee et al. (2016), Birid and Choudhury (2021), Keawsawasvong et al. (2022), and Yodsomjai et al. (2021a) reported that the behavior of these footings relies on the foundation's geometric size and soil properties. Specifically, clay, known for its strength anisotropy, was the focus of these investigations. Krabbenhoft et al. (2019) developed a novel failure criterion, termed the anisotropic undrained shear (AUS) model, akin to the formulations of Casagrande and Carrillo (1944) and Lo (1965). This model captures the intricate nature of anisotropic clay by utilizing the generalized Tresca criterion

* Corresponding author.
E-mail addresses: duy.tan@dome.tu.ac.th (D.T. Tran), jim.shiau@usq.edu.au (J. Shiau), divesh@tu.ac.th (D.R. Kumar), lvqui@hcmut.edu.vn (V.Q. Lai), ksurapar@engr.tu.ac.th (S. Keawsawasvong).

https://doi.org/10.1016/j.apor.2024.104375
Received 28 July 2024; Received in revised form 30 October 2024; Accepted 8 December 2024
Available online 13 December 2024

List of notations and symbols

Notations/symbol	Definition
3D AFELA	Adaptive three-dimensional finite element limit analysis
V	Vertical force
H	Horizontal force
M	Moment
r_i/r_o	The radius coefficient
r_e and r_s	Anisotropic strength factors/ The anisotropic ratio
s_{uTC}	Triaxial compressive undrained shear strength
s_{uTE}	Triaxial extension undrained shear strength
s_{uDSS}	Direct simple shear undrained shear strength
θ	Inclined angle
q_a	The uniaxial compression
r_i	An internal radius
r_o	An external radius
B	The outer diameter
A	The area surface
LRP	Load reference point
UB	Upper bound
LB	Lower bound
SOCP	Second order cone program
AUS	Anisotropic undrained shear
$V/s_{uTC}A$	The non-dimensional vertical load coefficient
$H/s_{uTC}A$	The non-dimensional horizontal load coefficient
$M/s_{uTC}AB$	The non-dimensional bending moment coefficient
V_0	The limiting vertical load ($H = M = 0$)
H_0	The ultimate horizontal load ($V = M = 0$)
M_0	The ultimate bending moment ($V = H = 0$)
V/V_0	Vertical load mobilization/ Normalized vertical load
H/H_0	Normalized horizontal load
M/M_0	Normalized bending moment
ANN	Artificial neural network
ABC	The artificial bee colony
ICA	The imperialist competitive algorithm
ALO	The artificial lion optimization
W	Weights
b	Biases
F_u	The yield function
LM	The Levenberg-Madquardt
SN	The number of solutions or population size
λ	Random number
fit_i	The fitness value of the i_{th} solution
y_{minj} and y_{maxj}	The boundaries for data points in the j_{th} dimension
N_{HL}	Hidden layer
N_h	Hidden neurons
N_P	A population or swarm size
I_{max}	Maximum iteration number of processing
x	The input data points
y	The output data points
N	The total data points
R^2	Coefficient of determination
RMSE	Root means square error
MAE	Mean absolute error
SSR	The sum of squares of the regression
SST	The total sum of squares
RMSD	Root mean square deviation

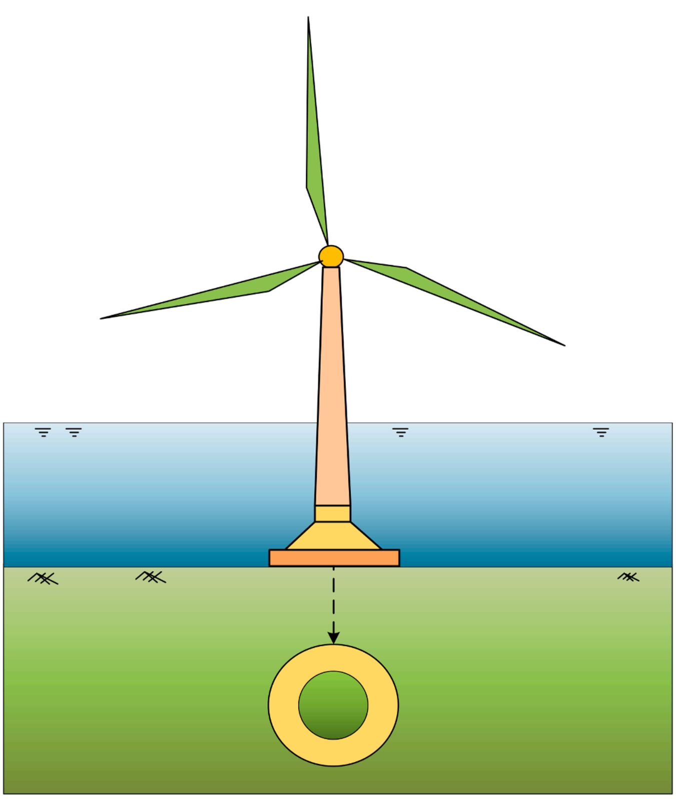

Fig. 1. Ring foundation as an offshore structure.

for undrained total stress analysis. Moreover, some researchers have developed new limit analysis solutions for determining the stability of foundations in anisotropic clays via the AUS model (e.g., Yodsomjai et al., 2021b; Ukritchon et al., 2020).

Previous studies have extensively analysed ring foundations under a single static load, unlike circular and square footings, which have been well studied with published results of failure envelopes in *V-H-M* space when under combined vertical (*V*), horizontal (*H*), and moment (*M*) loading conditions, ring foundations have yet to receive comparable attention. Although there have been comprehensive investigations into the failure envelopes of skirted shallow foundations under various loading conditions (e.g., Bransby and Randolph, 1998; Chanda et al., 2021; Gourvenec, 2008; Fiumana et al., 2019; Bransby and Yun, 2009; Mana et al., 2013; Zhuang et al., 2019; Liu et al., 2014; Shen et al., 2016; Dunne and Martin, 2017; Du et al., 2022; Liu et al., 2021; Zhao 2022 and 2024), most of them have focused on circular foundations, neglecting the effects of ring foundations under similar loading conditions.

Notably, there has not been any published work in the literature regarding the impact of anisotropy on the failure envelope of ring footings. This paper thus aims to study the failure envelopes of ring foundations of varying shapes and sizes placed on anisotropic clay. This research builds upon the prior work of Birid and Choudhury (2022) and Shen et al. (2016) to establish a new research framework. The failure loci developed here, termed AUS failure loci, offer valuable insights for designers to evaluate different load combinations under critical failure conditions. Any combination of vertical (*V*), lateral (*H*), and moment (*M*) loads falling within the presented failure locus is deemed safe for the foundation.

This study further utilizes machine learning methods such as artificial neural networks (ANNs) with their optimization performance through various models, such as ANN-ABC (artificial bee colony), ANN-ICA (imperialist competitive algorithm), and ANN-ALO (ant lion optimizer) (see, e.g., Le et al., 2019; Karaboga, 2005; Kumar et al., 2022;

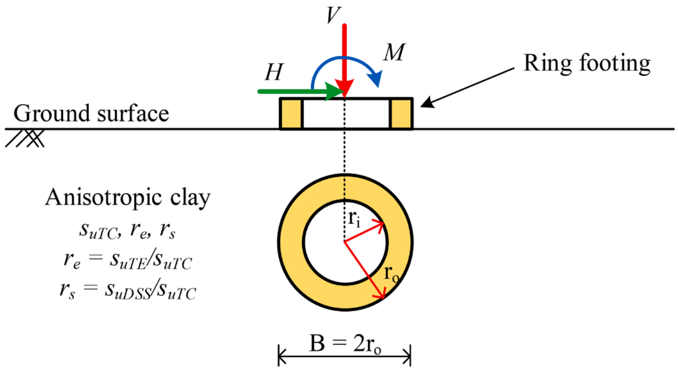

Fig. 2. Problem definition of a ring foundation under general loading.

Jitchaijaroen et al., 2023; Reddy, 2017; Keawsawasvong et al., 2023; Gholami et al., 2022; Tran et al., 2023; Panomchaivath et al., 2023). These techniques aim to develop an optimal predictive model for predicting the failure boundaries of ring foundations within complex engineering scenarios involving anisotropic clay in *V-H-M* space. Furthermore, no study has investigated the failure envelope's ring footing on anisotropic clay using AUS failure criteria combined with an artificial neural network algorithm. The research findings highlight the creation of an optimized predictive model tailored for addressing intricate challenges in engineering.

2. Problem statement

Fig. 2 shows the problem of a rigid ring foundation placed on the surface of an anisotropic ground. The ring foundation has an internal radius (r_i) and an external radius (r_o), and it is subjected to combined $V-H-M$ loads. The outer diameter $B = 2r_o$, the surface area $A = \pi(r_o^2\text{-}r_i^2)$, and the ratio between the internal and external radii (r_i/r_o) define the size of the ring foundation.

As stated by Krabbenhoft et al. (2015), the AUS failure criterion was specifically developed for anisotropic clays. Triaxial compression (s_{uTC}), triaxial extension (s_{uTE}), and direct simple shear (s_{uDSS}) are the three distinct anisotropic undrained shear strengths used to define AUS. Krabbenhoft et al. (2015) and Ladd (1991) identified two anisotropic strength ratios, r_e (s_{uTE}/s_{uTC}) and r_s (s_{uDSS}/s_{uTC}), on the basis of the three shear strengths. Their relationship is expressed through the harmonic mean of r_e and r_s, which is represented by $2r_e/(1+r_e) = r_s$. The influence of clay anisotropy is solely defined by the parameter r_e, which falls within the range of 0.5 to 1 (Krabbenhoft et al., 2015). The yield function (F_u) of the AUS model, which incorporates the harmonic mean of the triaxial shear strengths, is expressed as $F_u = \sigma_1\text{-}\sigma_3+(r_e\text{-}1)(\sigma_2\text{-}\sigma_3)-2s_{uTC} = 0$. Note that $\sigma_1 \geq \sigma_2 \geq \sigma_3$ represents the relationship between three principal stresses (positive in compression). When r_e equals 1 ($s_{uTC} = s_{uTE} = s_{uDSS}$), the failure criterion of the AUS model is the same as Tresca's failure criterion.

The numerical results of *V-H-M* are presented as dimensionless load parameters ($V/s_{uTC}A$, $H/s_{uTC}A$, and $M/s_{uTC}AB$) throughout the paper. To determine the respective uniaxial capacities, multiplier loads are applied to the ring footing surface in the corresponding directions. Various combinations of *V-H*, *V-M*, and *H-M* loads thus created failure boundaries for different scenarios. For example, *V-H* and *V-M* cases were examined in planes where *M* or *H* was zero, respectively, whereas *H-M* scenarios were explored when *V* was zero. In cases of combined *V-H-M* loading, portions of the vertical capacity were distributed ($V/V_0 = 0$, 0.25, 0.5, and 0.75) onto the ring foundation surface, followed by various fixed ratios of *H-M* loads to assess different *H-M* combinations at failure under varying vertical loads. This approach has been well documented in the literature by Gourvenec and Randolph (2003), Bransby and Randolph (1998), Tan (1990), Chen et al. (2022), and Shen et al. (2016).

Factors such as the anisotropic strength ratio (r_e), radius ratio (r_i/r_o), and vertical load mobilization (V/V_0) all influence the configurations of the $V-H$, $V-M$, and $H-M$ failure envelopes. Moreover, normalization of the $H-M$ failure envelope relies on the maximum horizontal and moment capacities that are decreased by the applied vertical and horizontal loads. This reduction changes the dimensions of the $H-M$ failure envelope. Applying the Butterfield (1999) dimensionless approach reveals that two dimensionless input factors predominantly lead to the normalized output outcomes (*V-H-M*) represented in Eq. (1).

$$\frac{V}{s_{uTC}A},\frac{H}{s_{uTC}A},\frac{M}{s_{uTC}AB} = f\left(\frac{r_i}{r_o}, r_e\right) \tag{1}$$

Table 1
Summary of the dimensionless vertical ultimate load $V_0/s_{uTC}A$ for a ring foundation in anisotropic clay.

r_e	0.5	0.6	0.7	0.8	0.9	1
$r_i/r_o = 0$	4.95	5.28	5.57	5.75	5.94	6.06
$r_i/r_o = 0.2$	4.58	5.02	5.33	5.6	5.82	6.04
$r_i/r_o = 0.4$	3.96	4.43	4.84	5.21	5.53	5.84
$r_i/r_o = 0.6$	3.77	4.27	4.68	5.1	5.47	5.76

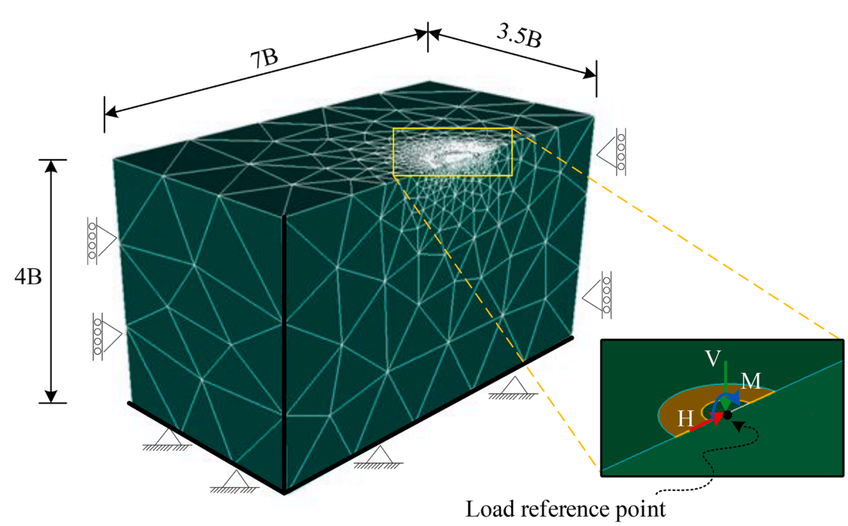

Fig. 3. Problem domain showing the adaptive mesh design and boundary conditions.

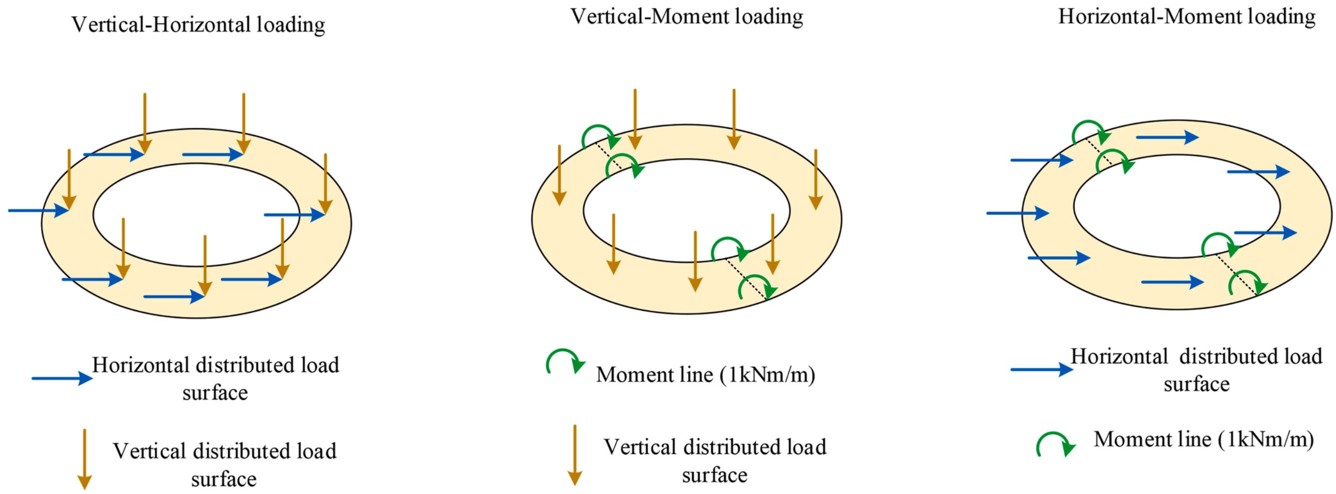

Fig. 4. Illustration of *V−H, V−M*, and *H−M* loadings (after Birid and Choudhury, 2022).

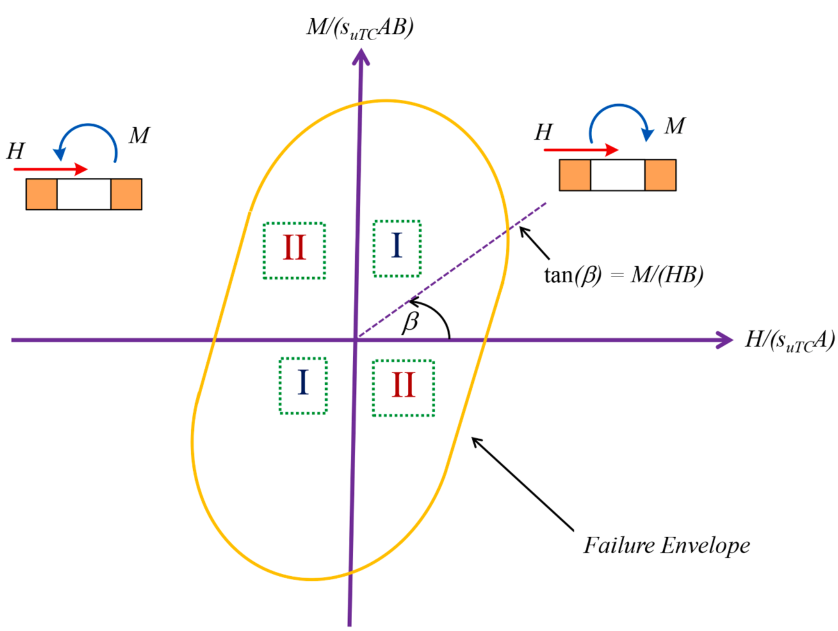

Fig. 5. Analysis of the 2D failure envelope for a given V/V_0 value.

Table 2
Parameter ranges for the input.

Variable	Selected values
r_i/r_o	0, 0.2, 0.4, 0.6
r_e	0.5, 0.6, 0.7, 0.8, 0.9, 1
V/V_0	0, 0.25, 0.5, 0.75
β	0°, 15°, 30°, 60°, 90°, 100°, 120°, 140°, 160°, 180°

where the radius ratio is denoted as (r_i/r_o) and the anisotropic strength coefficient is presented as (r_e). The specified dimensionless values for these parameters in the research are $r_i/r_o = 0$, 0.2, 0.4, 0.6, and $r_e = 0.5$, 0.6, 0.7, 0.8, 0.9, and 1. In detail, the values of the input geometry parameters for r_i/r_o refer to the work of Birid and Choudhury (2022), whereas the anisotropy ratio r_e follows the theory of the AUS soil presented by Krabbenhoft et al. (2019) and Keawsawasvong et al. (2022). The AUS model has been highlighted in previous studies by Yodsomjai et al. (2021b) and Ukritchon et al. (2020).

To construct a 3D failure envelope using dimensionless variables ($V/s_{uTC}A$, $H/s_{uTC}A$, $M/s_{uTC}AB$), the dimensionless vertical load factor, $V/s_{uTC}A$, is split into two components: the ratio of vertical load mobilization levels (V/V_0) and $V_0/s_{uTC}A$, as described in Eq. (2).

$$\frac{V}{s_{uTC}A} = \frac{V}{V_0} \times \frac{V_0}{s_{uTC}A} \tag{2}$$

The value of V_0 represents the maximum load that a ring footing can sustain under pure vertical loading (pure V) for each soil profile. Determining the $V_0/s_{uTC}A$ value before conducting failure envelope analysis is essential. Once $V_0/s_{uTC}A$ is established, the value of $V_0/s_{uTC}A$ is obtained by multiplying it by the V/V_0 value within the range [0, 0.25; 0.5; 0.75; 1]. Consequently, the $V/s_{uTC}A$ value ranges from 0 to $V_0/s_{uTC}A$. Based on this adjustment, the previously analysed 3D failure envelope ($V/s_{uTC}A$, $H/s_{uTC}A$, $M/s_{uTC}AB$) is now transformed into the 3D failure envelope (V/V_0, $H/s_{uTC}A$, $M/s_{uTC}AB$), as described earlier by Gourvenec et al. (2011) and Taiebat and Carter (2000).

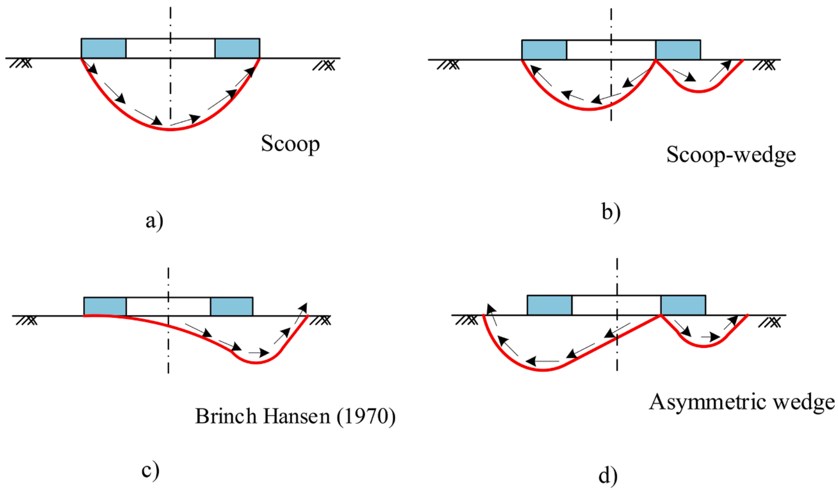

Fig. 6. Examination of the failure mechanisms for $H-M$ loading with (a) scoop, (b) scoop-wedge, (c) Brinch Hansen (1970), and (d) asymmetric wedge.

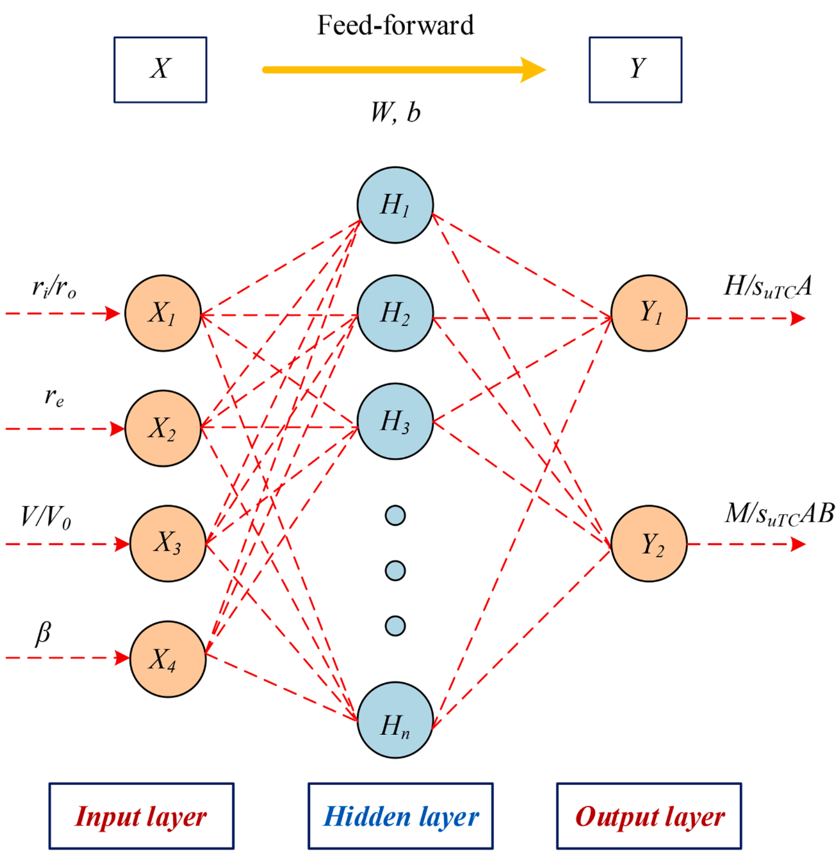

Fig. 7. Model architecture for an ANN (Artificial Neural Network).

3. Methodology

3.1. Finite element limit analysis (FELA)

The FELA technique provides remarkable precision and accuracy in its lower and upper bound results, providing an estimate close to the exact value (Sloan, 2013; Krabbenhoft et al., 2015). The lower bound (LB) analysis defines the soil mass using triangular elements with three unknown stresses assigned to each node. Stress discontinuity is allowed along the shared edges of surrounding components, especially interfacial aspects, by modelling each triangle element with its unique nodes. The computation of the lower bound involves a second-order cone program (SOCP) that satisfies equilibrium equations, stress boundary conditions, and yield criteria. This problem aims to determine the ultimate pressure influenced by optimizing these unknown stresses. On the other hand, upper limit calculations involve structuring the soil mass around the foundation into triangular pieces with six nodes, each connected to two unknown velocities. The velocities are computed within each element using a quadratic formula. While allowing velocity discontinuities to reach soil footing interfaces, the upper bound computation formulates a kinematically acceptable velocity field, satisfying boundary conditions and compatibility equations to minimize the ultimate pressure. The virtual work concept is utilized in the upper bound solution, contrasting external load work with internal energy dissipation

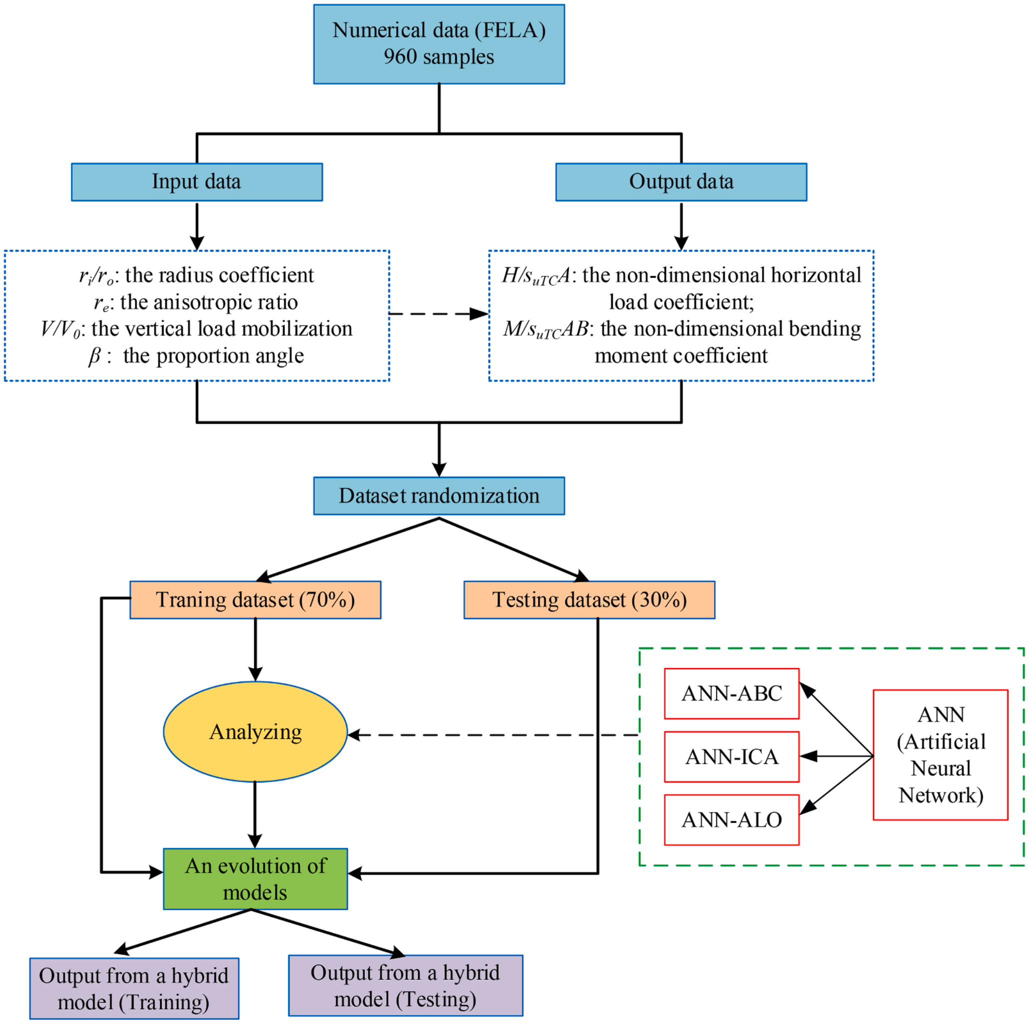

Fig. 8. Flow diagram showing the development of an ANN-hybrid model.

Table 3
Statistical details of the variables used in the failure envelope analysis.

Index	r_i/r_o	r_e	V/V_O	β	$H/s_{uTC}A$	$M/s_{uTC}AB$
Minimum	0.0	0.5	0.0	0.0	−1.204	0.0
Maximum	0.6	1	0.75	180	1.205	1.537
Mean	0.3	0.75	0.375	89.5	0.029	0.406
Median	0.3	0.75	0.375	95	−0.017	0.391
Standard Deviation	0.223	0.171	0.279	58.93	0.683	0.305
Kurtosis	−1.36	−1.27	−1.36	−1.28	−1.24	0.565
Skewness	0.0	0.0	0.0	−0.057	0.077	0.696

Table 4
Hyperparameters in the hybrid ANN model.

Hybrid ANN models	Hyperparameters					
	N_{HL}	N_h	N_P	I_{max}	UB	LB
ANN-ABC	1.0	5, 6, 7, 8, 9, 10	30	10,000	1.0	−1.0
ANN-ICA	1.0	5, 6, 7, 8, 9, 10	30	10,000	1.0	−1.0
ANN-ALO	1.0	5, 6, 7, 8, 9, 10	30	10,000	1.0	−1.0

at triangular interfacial parts, according to Sloan (2013) and Krabbenhoft et al. (2015).

The model geometry for this problem is shown in Fig. 3, which shows a half-cut view of a ring foundation on clay. The modelling involved the use of rigid plate elements with a thickness of 0.2 m for the ring footing and solid components to represent the clay layer. Different ring foundations are considered with varying inner-to-outer radius ratios (r_i/r_o) of 0, 0.2, 0.4, and 0.6 for the circular rigid shells. The AUS model is employed as a failure criterion for anisotropic clay. Various soil types with anisotropic values ranging from $r_e = 0.5$ to 1 are considered. The interface between the bottom of the ring foundation and the soil was assumed to be fully rough, ensuring complete bonding between the footing and the soil. It is further emphasized that the assumptions are built on previous studies on circular and ring foundations, as presented by Gourvenec and Randolph (2003), Gourvenec et al. (2011), and Birid and Choudhury (2022). A sufficiently large domain size is used to eliminate possible boundary effects. In this case, the soil domain is 7B in width, and the depth is 4B below the soil surface with a constant outer diameter (B) of 1.0 m, providing ample area for failure mechanisms to fully take effect. The load reference point (LRP) can be positioned at the midpoint of the foundation at the ground level when $r_i/r_o = 0$. The side boundaries were constrained against lateral deformation but allowed free vertical displacement. The model's bottom edge was fixed to prevent lateral and vertical displacement, as indicated in Fig. 3. The mesh underwent three adaptive refinement steps, starting with 5000 elements and ending with 10,000 elements. This is considered as a good balance between computational efficiency and accuracy (e.g., Xiao et al., 2018; Chen and Liu, 2018; Zhang et al., 2022; Yu et al., 2018; Payan et al., 2022; Shiau et al., 2000 and 2018). This method automatically refines

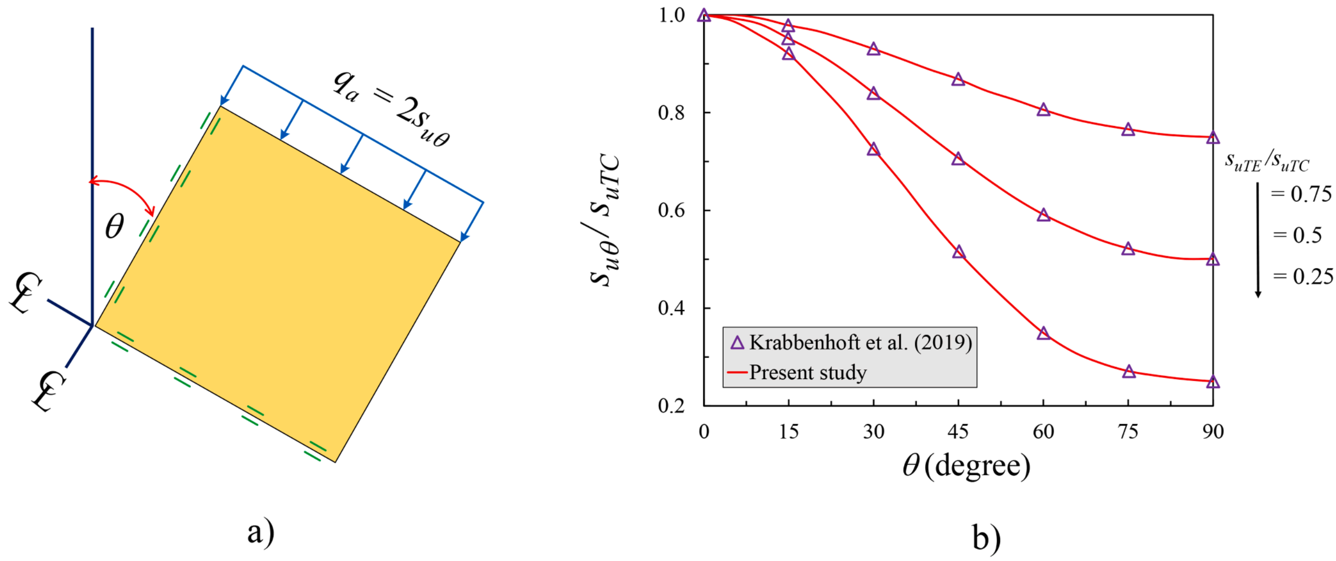

Fig. 9. Validation of FELA application with the AUS failure criterion with (a) model specifics and (b) verification.

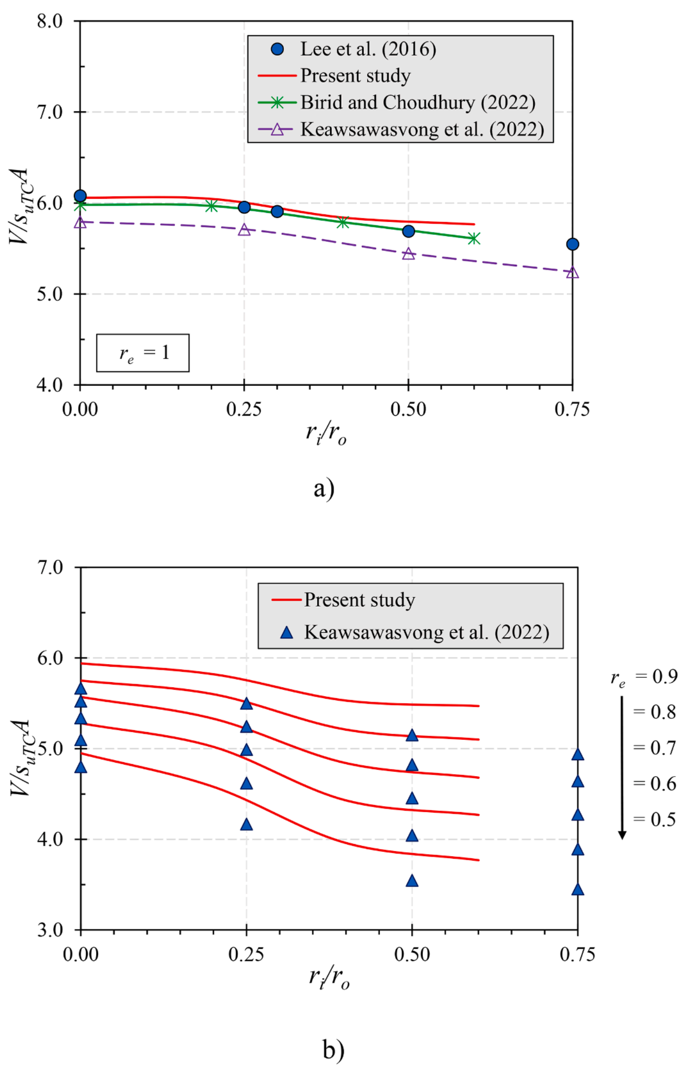

Fig. 10. Comparison of the results with those of existing studies on ring foundations resting on (a) isotropic clay and (b) anisotropic clay.

the mesh by increasing the density in regions with high plastic shearing strain. Specifically, the initial and target number of elements, the number of adaptive iterations, and the adaptivity control parameter (such as shear dissipation) must be defined (Krabbenhoft et al., 2015). Initially, the mesh size distribution is set based on the initial number of elements specified by the user. Next, the mesh is generated according to the defined distribution. Then, the limit analysis problem is solved using finite element discretization on the mesh. If convergence is achieved, the adaptivity process is complete; if not, the mesh refinement technique adjusts the mesh size distribution and then returns to the initial step (Ciria et al., 2008). Notably, both fixed and multiplier load concepts are essential for applying and analysing simulations using Optum G3 (Krabenhoft et al., 2015). A fixed load is a constant load applied to a structure and does not change in magnitude or direction during the analysis or throughout the loading process (e.g., gravity load, self-weight of a structure, or soil pressure). On the other hand, a multiplier load, or variable load, changes in magnitude based on a specified factor or set of conditions and often varies to simulate different scenarios or loading conditions (e.g., wind load, earthquake forces, and wave load). It can be adjusted to determine the load at which failure occurs and is often used in limit analysis to determine the ultimate load–carrying capacity of OptumG3 (Krabenhoft et al., 2015). Multiplier loads are essential for parametric studies and stability analysis, helping find the load factor at which the system reaches its limit state and providing insight into the safety and design requirements. This methodology has been widely applied to several geotechnical stability problems by Shiau et al. (2018, 2022, 2023).

In view of the computation process, the limit load (V_0) was initially assessed under a solely vertical load condition before proceeding with the *V-H* analysis (Tan, 1990). This process yields the limiting vertical loads (V_0) for different r_e and r_i/r_o values, as shown in Table 1. The *V-H* load combination analysis was then followed by applying a fixed horizontal distributed load while optimizing the vertical limit load (V). The fixed horizontal load was subsequently varied, and new reduction factors for the pure vertical limit load were subsequently determined. This process ultimately generates the *V*−*H* plot by repeating the fixed horizontal loads. Similar analyses were conducted to create *V-M* failure boundaries on the centreline of the footing. These solutions have been explained by Birid and Choudhury (2022). Specifically, the analyses involved applying horizontal loads in both the positive and negative directions, with the moment used solely in the positive direction to produce *H-M* failure, as shown in Fig. 4. Note that the unit moment (1 kNm/m) was applied along the centerline of the ring footing.

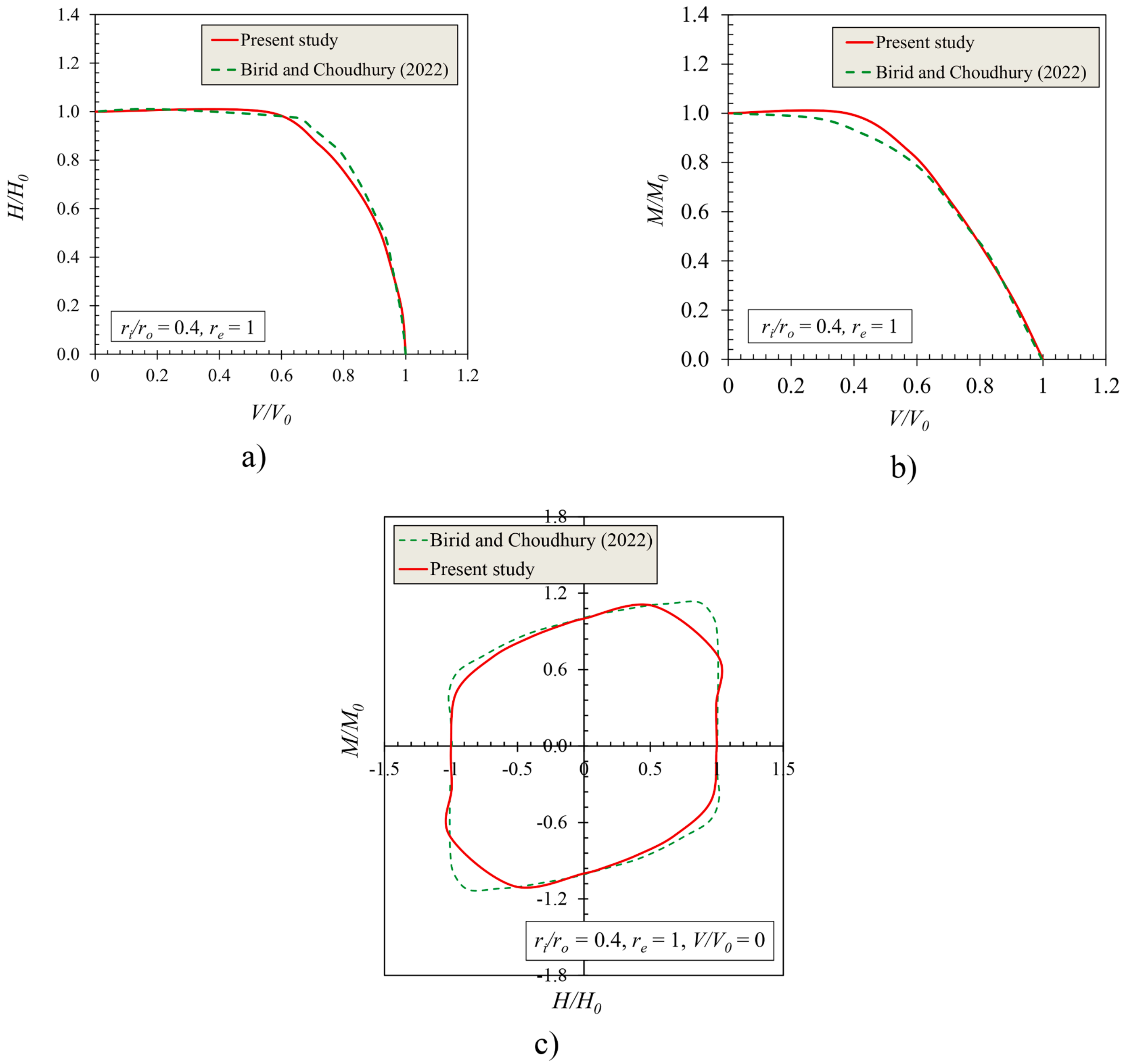

Fig. 11. Comparison of *the* V–H–M failure envelopes between the current study and those in Birid and Choudhury (2022) with (a) V–H loading, (b) V–M loading, and (c) H–M loading.

To simulate combined V–H–M loading, a percentage of the vertical capacity ($V/V_0 = 0$, 0.25, 0.5, and 0.75) was applied to the surface of the ring foundation as a distributed load. At a certain value of V/V_0, it can be seen as a two-dimensional failure envelope in the H-M space ($H/s_{uTC}A$, $M/s_{uTC}AB$). Fig. 5 shows the analysis of two distinct situations for each envelope in the ($H/s_{uTC}A$, $M/s_{uTC}AB$) space. In quadrant I, the lateral load and bending moment cause the footing to topple in the same direction. In a separate instance, shown as (II) in the second quadrant, the rotational motion occurs in opposing directions as a result of the disparity between the lateral load and bending moment, as highlighted in a previous study conducted by Keawsawasvong and Ukritchon (2016). The remaining plots in the third and fourth quadrants can be obtained using problem anti-symmetry, which means that the outcomes in the first and second quadrants are mirrored in the third and fourth quadrants (see Fig. 5).

To construct a 3D failure envelope, the initial step involves determining the 2D failure envelope for four different cross-sections of $V/V_0 = 0$, 0.25, 0.5, and 0.75, using the dimensionless parameters $H/s_{uTC}A$ and $M/s_{uTC}AB$. When attempting to establish the 2D failure envelope in the $H/s_{uTC}A$ - $M/s_{uTC}AB$ space, it is necessary to determine the relationship between the horizontal load and bending moment using the equation $\tan(\beta) = M/(HB)$. The value of β denotes the angle measured from the positive direction of the horizontal axis, as shown in Fig. 5 (Salencon and Peeker 1995). This study selects the value of β as the loading limit for the FELA, which is within the range of 0 to 180°. Table 2 illustrates the total number of 960 (4 × 6 × 4 × 10) analysis cases with ranges of (r_i/r_o, r_e, V/V_0, β) to compute ($H/s_{uTC}A$, $M/s_{uTC}AB$). The failure envelopes for ring foundations can be normalized by the ultimate values V_0, H_0, and M_0 and are reported as V/V_0, H/H_0, and M/M_0, respectively (Gourvenec and Randolph, 2003; Gourvenec, 2008; Birid and Choudhury, 2022). The ultimate loads refer to the loads that occur when there is pure loading, such as when $H = M = 0$ for V_0, $M = V$

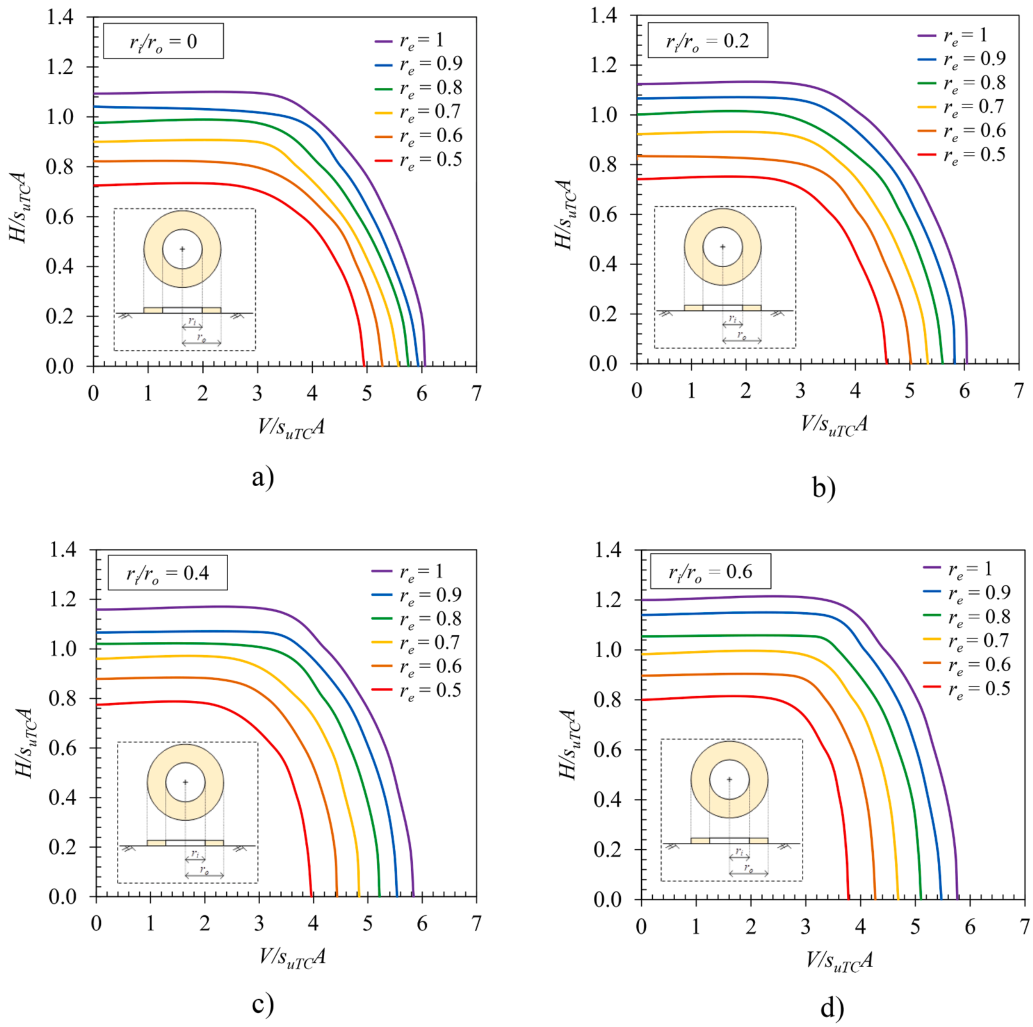

Fig. 12. Failure envelope under *V-H* loading with (a) $r_i/r_o = 0$, (b) $r_i/r_o = 0.2$, (c) $r_i/r_o = 0.4$, (d) $r_i/r_o = 0.6$.

$= 0$ for H_0, and $V = H = 0$ for M_0.

A schematic of the scoop mechanism is shown in Fig. 6(a). As the horizontal load increases and the moment capacity decreases, the scoop decreases, and the wedges extend across the foundation base, transitioning into a sliding mechanism. For vertical load mobilization on a ring foundation, failure dominated by a moment rather than a horizontal load appears as a scoop–wedge mechanism (Fig. 6b). After the maximum moment is mobilized, a Brinch Hansen mechanism is generated, as shown in Fig. 6c (Brinch Hansen, 1970; Gourvenec, 2007). Failure more strongly influenced by the horizontal load than the moment results in an asymmetric wedge mechanism, as shown in Fig. 6d. An examination of the failure mechanism of a ring footing under combined loading highlights the novelty and originality of this study.

3.2. Artificial neural network (ANN) and hybrid ann optimization

An artificial neural network (ANN) imitates the human mind's organization with the arrangement of biological neural networks. Several studies, including those by Rabi et al. (2023), Nguyen et al. (2023), Kumar and Samui (2008), Armaghani et al. (2015), and Kumar et al. (2022), have highlighted the importance of using ANNs across different civil engineering applications. Fig. 7 shows a typical structure of a feed-forward network comprising input, hidden, and output layers. Note that each node within carries its weights (*W*) and biases (*b*) that are adjusted during training via the Levenberg−Madquardt (LM) backpropagation algorithm (Hagan et al., 1994). Each hidden node uses a non-linear activation function, which is typically either sigmoid or hyperbolic tangent (tanh or tansig). These functions, known for enhancing convergence speed and model performance, are employed for the linear transfer functions of the hidden and output layers, respectively (Sirimontree et al., 2022). This research uses both activation functions to build artificial neural network (ANN) models according to Eq. (3).

$$Output = \sum_{i=1}^{N_h} \mathrm{W}^{2,i}\mathrm{tansig}\left(\sum_{j=1}^{J} \mathrm{W}^{1,i}\mathrm{x}^{j} + \mathrm{b}^{1,i}\right) + \mathrm{b}^{2,i} \quad (3)$$

In this work, artificial neural networks are used to calculate the failure envelope ($H/s_{uTC}A$, $M/s_{uTC}AB$) for a ring footing on anisotropic clay subjected to combined loading. The correlation equations derived from this approach enable practitioners to efficiently determine the 3D failure envelope (V/V_0, $H/s_{uTC}A$, $M/s_{uTC}AB$) in the *V-H-M* space. The inputs for the ANN model consist of parameters such as (r_e), vertical load mobilization (V/V_0), the proportion angle (β), and various (r_i/r_o) radius ratios. More detailed information on the use of the Levenberg−Madquardt (LM) algorithm to train feedforward networks can be found in Marquardt (1963) and Hagan et al. (1994).

To optimize artificial neural network models, three unique combinations of soft computing techniques, namely, artificial neural networks with an artificial bee colony (ANN-ABC), artificial neural networks with an imperialist competitive algorithm (ANN-ICA), and artificial neural networks with an ant lion optimizer (ANN-ALO), are adopted in this paper to assess the failure contour of a ring footing on anisotropic clay.

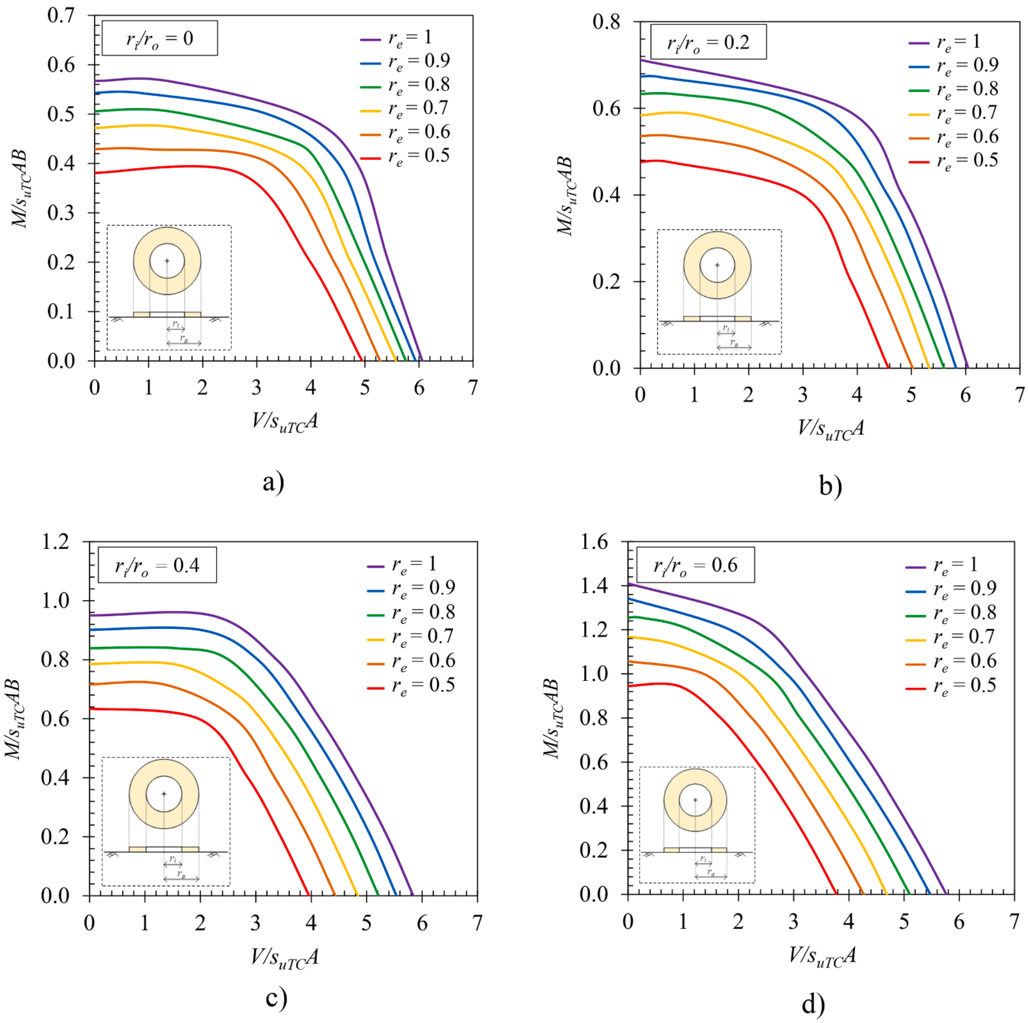

Fig. 13. Failure envelopes under *V-M* loading with (a) $r_i/r_o = 0$, (b) $r_i/r_o = 0.2$, (c) $r_i/r_o = 0.4$, (d) $r_i/r_o = 0.6$.

These methods have been well addressed in earlier studies by Le et al. (2019), Sangjinda et al. (2024) and Kumar et al. (2022). In brief, the ABC optimization algorithm, inspired by nature and introduced by Karaboga (2005), is a swift and straightforward method in AI and is a metaheuristic optimization approach that handles discrete and continuous problem types. Within this algorithm, three population categories exist: hired bees, spectator bees, and scout bees, each starting from different initial positions.

The "hired bees" gather resources from identified sources and communicate with spectator bees, and then spectator bees synthesize information from the hired bees to make decisions regarding these food sources. Once the employed bees deplete a source, spectator bees transform into scouting bees, seeking out new, arbitrary sources. This technique creates a dispersed population of SN solutions, where SN represents the number of solutions or population size, via a randomized approach outlined in Eqs. (4) to (6).

$$y_{i,j} = \mathrm{rand}[0,1] \times \left(y_{maxj} - y_{minj}\right) + y_{minj} \tag{4}$$

$$p_{i,j} = \frac{\mathrm{fit}_i}{\sum_{i=1}^{N} \mathrm{fit}_i} \tag{5}$$

$$v_{i,j} = \lambda \times \left(y_{i,j} - y_{t,j}\right) + y_{i,j} \tag{6}$$

where $y_{i,j}$ represents the population count of the j_{th} parameter within the i_{th} solution, with y_{minj} and y_{maxj} setting the boundaries for y_i in the j_{th} dimension; λ represents a random number within the range of −1 to 1, fit_i denotes the fitness value of the i_{th} solution.

The imperialist competitive algorithm (ICA) is a method for optimizing solutions inspired by social and political systems, particularly the dynamics between imperialist powers and their colonies. ICA utilizes a balance factor to control how much it explores versus exploits, enabling adjustments for optimizing this trade-off. Through numerous iterations, ICA refines solutions, fostering a dynamic interplay between competition and cooperation, ultimately reaching a satisfactory solution (Le et al., 2019; Atashpaz-Gargari and Lucas, 2007).

The ALO algorithm draws inspiration from the distinctive behavior of antlion larvae during their food search, a concept introduced by Mirjalili (2015). It employs a meta-heuristic process utilizing a stochastic population-based optimization technique known for its exceptional ability to solve many optimization problems. This technique models the objective function to mirror the hunting process of antlions, employs six operations that mimic the actions undertaken by these insects during their hunt, and an optimization model is constructed. Specifically, the ALO algorithm is utilized to increase the performance of an artificial neural network (ANN) by adjusting the weight and bias values of the ANN. Furthermore, the ALO method serves as a solution for complex engineering challenges, functioning as a global search optimization strategy, as highlighted by Mirjalili et al. (2017). For an in-depth understanding of the developed algorithm, interested individuals can refer to literature sources such as Mirjalili (2015) and Narasimhulu et al.

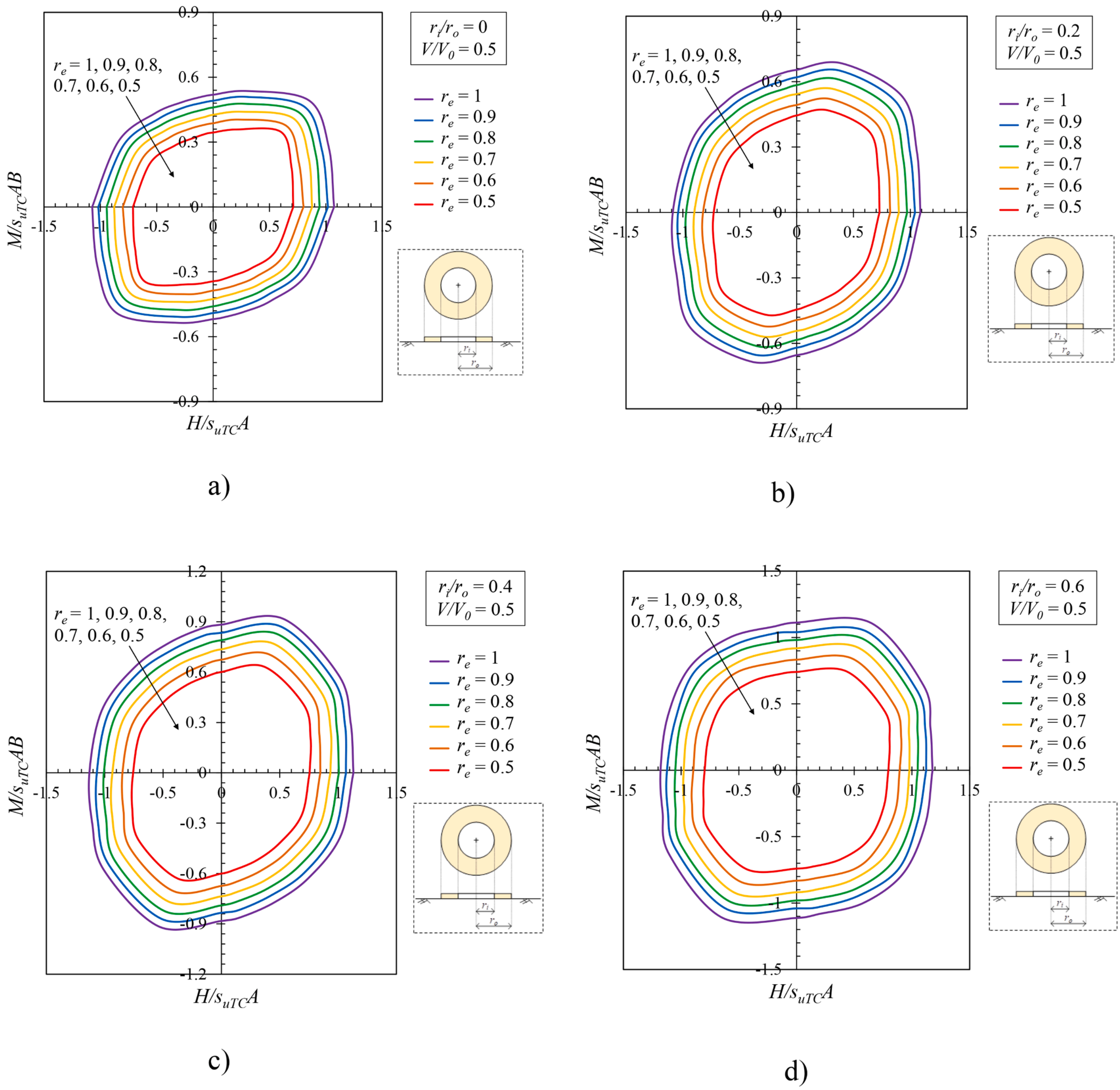

Fig. 14. Failure envelope of the ring footing for combined loading analysis under $H-M$ loading for $V/V_0 = 0.5$ and (a) $r_i/r_o = 0$, (b) $r_i/r_o = 0.2$, (c) $r_i/r_o = 0.4$, and (d) $r_i/r_o = 0.6$.

(2020). The study integrates three optimization methods (i.e., ABC, ICA, and ALO) with an ANN model and evaluates the performance of each resulting model. The flow chart presented in Fig. 8 illustrates the model's development process.

In this study, the numerical data are split randomly into two segments: training and testing sets, in which 70 % (672 data points) of the entire dataset is chosen randomly and 30 % (288 data points) is set aside for testing the developed models (Kumar et al., 2024). Thus, the plots of all the considered input parameters, including the radius factor (r_i/r_o), the anisotropic ratio (r_e), the vertical load mobilization (V/V_0), the proportion angle (β), and the output parameters $H/s_{uTC}A$ and $M/s_{uTC}AB$, are prepared for each variable. Details about the descriptive statistics of the dataset used are crucial to understanding the data pattern that is utilized in the numerical analysis and construction of machine learning models. In this section, the details of the descriptive statistics for the failure envelope of the ring foundation are presented in Table 3.

The ANN model employs a hidden layer (N_{HL}) with the number of hidden neurons (N_h) ranging from 5 to 10. The activation functions use a hyperbolic tangent for the hidden layer and a linear function for the output layer. The optimization algorithm is characterized by hyperparameters such as a population or swarm size (N_P) of 30, a maximum of 10,000 iterations (I_{max}), and weight and bias values constrained between −1 and 1 for both the lower and upper bounds (LB and UB). This study avoided overfitting and underfitting by utilizing hyperparameter tuning, stopping early, and defining specific convergence criteria for the hybrid ANN models. By carefully adjusting these aspects, optimal model performance was achieved, resulting in a reliable and generalizable solution. Table 4 outlines the configuration of all the hybrid ANN models used in this study.

The performance of the created models was assessed using two sta-

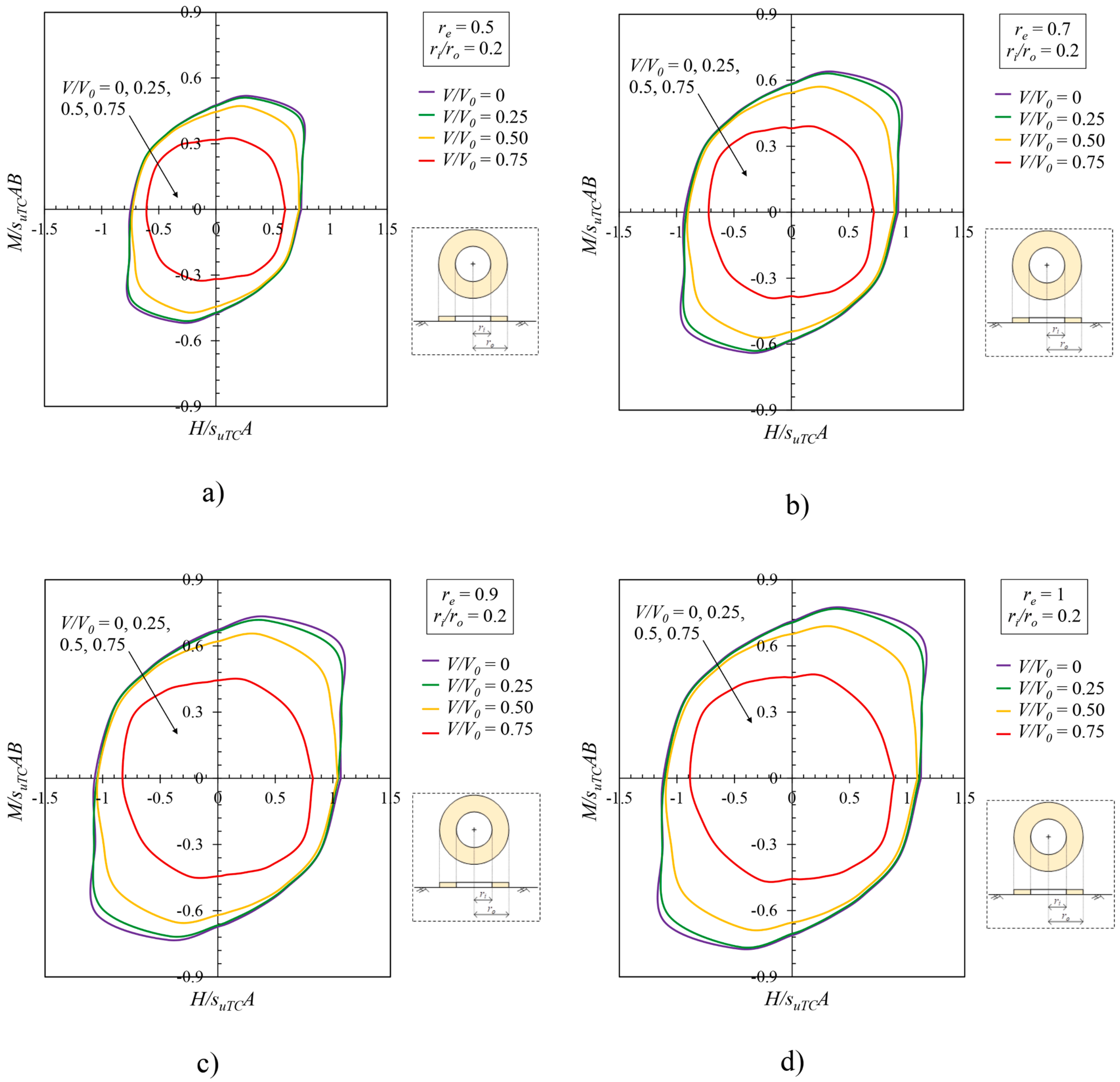

Fig. 15. 2D diagram representation of the combined failure loads for a ring foundation with $r_i/r_o = 0.2$ and (a) $r_e = 0.5$, (b) $r_e = 0.7$, (c) $r_e = 0.9$, (d) $r_e = 1$.

tistical measures. Each ANN model's performance is subsequently evaluated using statistical metrics such as the root mean square error (*RMSE*) and coefficient of determination (R^2), as indicated in Eqs. (7) and (8).

$$\mathrm{R}^2 = 1 - \frac{\mathrm{SSR}}{\mathrm{SST}} \tag{7}$$

$$\mathrm{RMSE} = \sqrt{\frac{1}{N}\sum_{i=1}^{N}(\mathrm{y_i} - \mathrm{f(x_i)})^2} \tag{8}$$

Here, *SSR* signifies the sum of squares of the regression, while *SST* represents the total sum of squares. N represents the total number of data points, with y_i being the targets and $f(x_i)$ being the model outputs. As R^2 approaches one and *RMSE* decreases, the relationship between the output and the target becomes stronger, indicating a closer association.

4. Verification

The initial comparison set validates the Finite Element Limit Analysis (FELA) using the Anisotropic Undrained Shear (AUS) failure criterion. Validation is achieved by analyzing a plane strain square block inclined at angle θ relative to the vertical axis and subjected solely to uniaxial compression (q_a) along the inclined direction, as illustrated in Fig. 9(a). Due to the symmetry of the setup, only a quarter of the square block is modeled in FELA. Given the constant stress state within the problem, a coarse, uniformly distributed mesh is sufficient for simulating the plane strain block. Boundary conditions for this symmetric block are specified in Fig. 9(a), and the simulation's objective is to maximize compressive traction q_a that leads to block failure. The inclined block is evaluated for θ values of 0, 15, 30, 45, 60, 75, and 90°. The s_{uDSS} value is approximated for verification as the average of s_{uTC} and s_{uTE}. Analytical solutions by Krabbenhoft et al. (2019) are referenced, with anisotropic strength

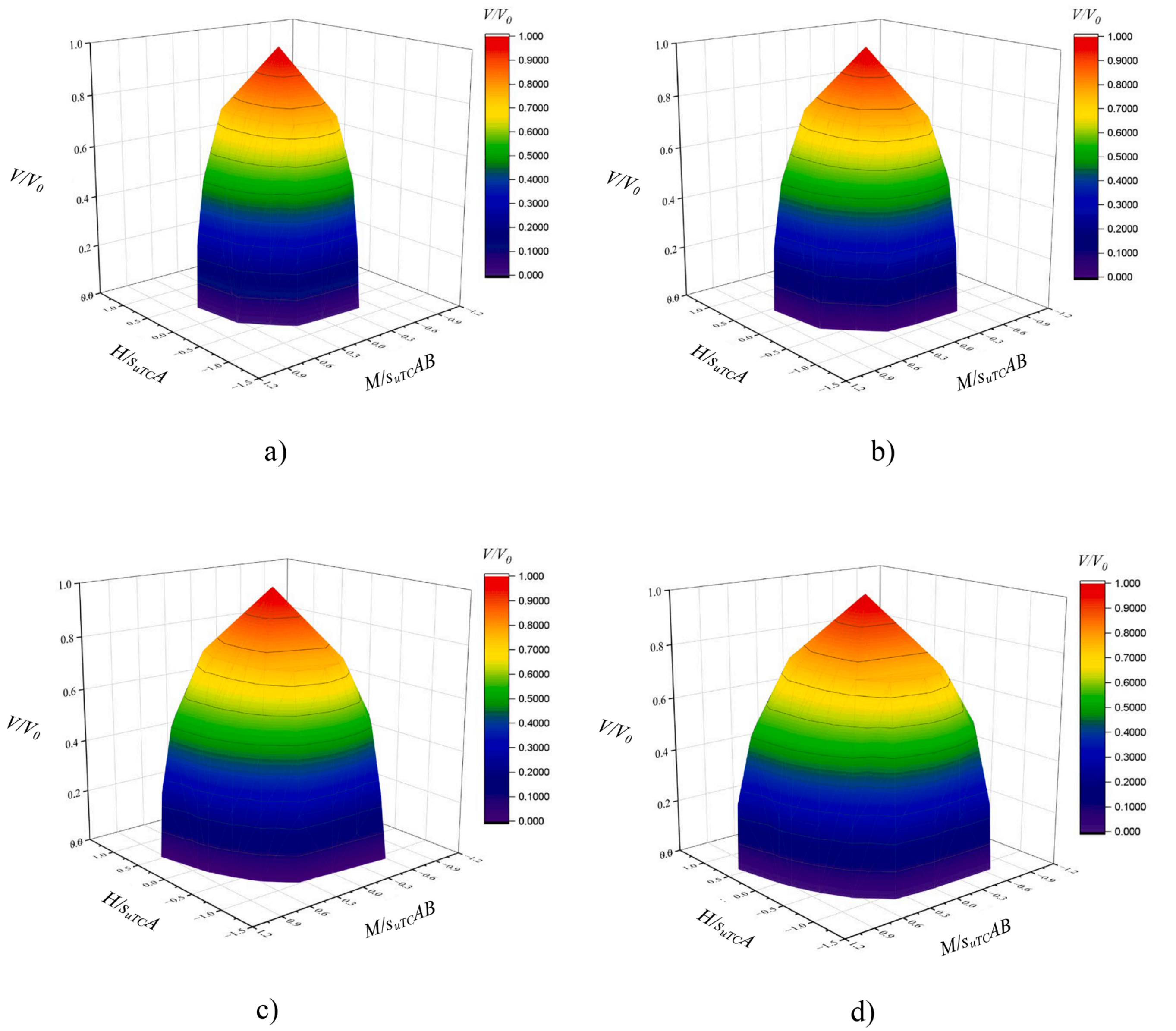

Fig. 16. 3D diagram representation of the combined failure loads for a ring foundation with $r_i/r_o = 0.4$ and (a) $r_e = 0.5$, (b) $r_e = 0.6$, (c) $r_e = 0.8$, (d) $r_e = 1$.

ratios of s_{uTE}/s_{uTC} set to 0.25, 0.5, and 0.75 for validation. Fig. 9(b) shows excellent agreement in undrained shear strength $s_{u\theta}$ between Krabbenhoft et al. (2019) analytical solutions and the current FELA simulations for inclined block compression across all strength ratios and orientation angles, validating the effectiveness of FELA with the AUS failure criterion.

The validation of the calculated solutions for the vertical bearing capacity factor obtained from the present study for ring footing resting on isotropic clay ($r_e = 1$) and anisotropic clay ($r_e = 0.5$ to 0.9) is shown in Fig. 10. The verification process includes the examination of the solutions proposed by Lee et al. (2016) using the finite element method (FEM), the finite element limit approach introduced by Birid and Choudhury (2022), and the two-dimensional finite element limit analysis conducted by Keawsawasvong et al. (2022) under axisymmetric conditions. Fig. 10a shows that the current solutions are slightly greater than the earlier solutions by Birid and Choudhury (2022) and Keawsawasvong et al. (2022) because different mathematical types for failure criteria were employed. Nevertheless, the outcome closely corresponds to the findings of Lee et al. (2016). In Fig. 10b, the results are compared with those of Keawsawasvong et al. (2022) for cases with ($r_e = 0.5$ to 0.9 and $r_i/r_o = 0.2$ to 0.6). The comparison shows a close alignment between present results and Keawsawasvong et al. (2022) across all scenarios, with differences ranging from 4 to 7 %. The proposed method can be deemed highly effective, as it results in a percentage difference of <7 % compared with previous investigations.

In this verification section, the normalized failure envelopes for *V-H*, *V-M*, and *H-M* load combinations are compared with those proposed by Birid and Choudhury (2022) to validate the numerical model. The comparison is presented in Figs. 11(a-c) for the case of isotropic clays with $r_e = 1$. Note that the AUS failure criterion is equivalent to the Tresca failure criterion when $r_e = 1$.

The first validation involves examining the $V-H$ failure envelope of the ring footing on isotropic clay, with r_i/r_o values of 0.4 and r_e value of 1. This is shown in Fig. 11(a). The numerical results show that the present solutions are similar to those of Birid and Choudhury (2022) by approximately 2.8 %. The second verification involves examining the $V-M$ failure envelope of the ring footing. In this case, the ratio of the inner radius to the outer radius (r_i/r_o) is 0.4, and the equivalent radius (r_e) is 1, as depicted in Fig. 11(b). The results again show that the present solutions are consistently greater than those of Birid and Choudhury

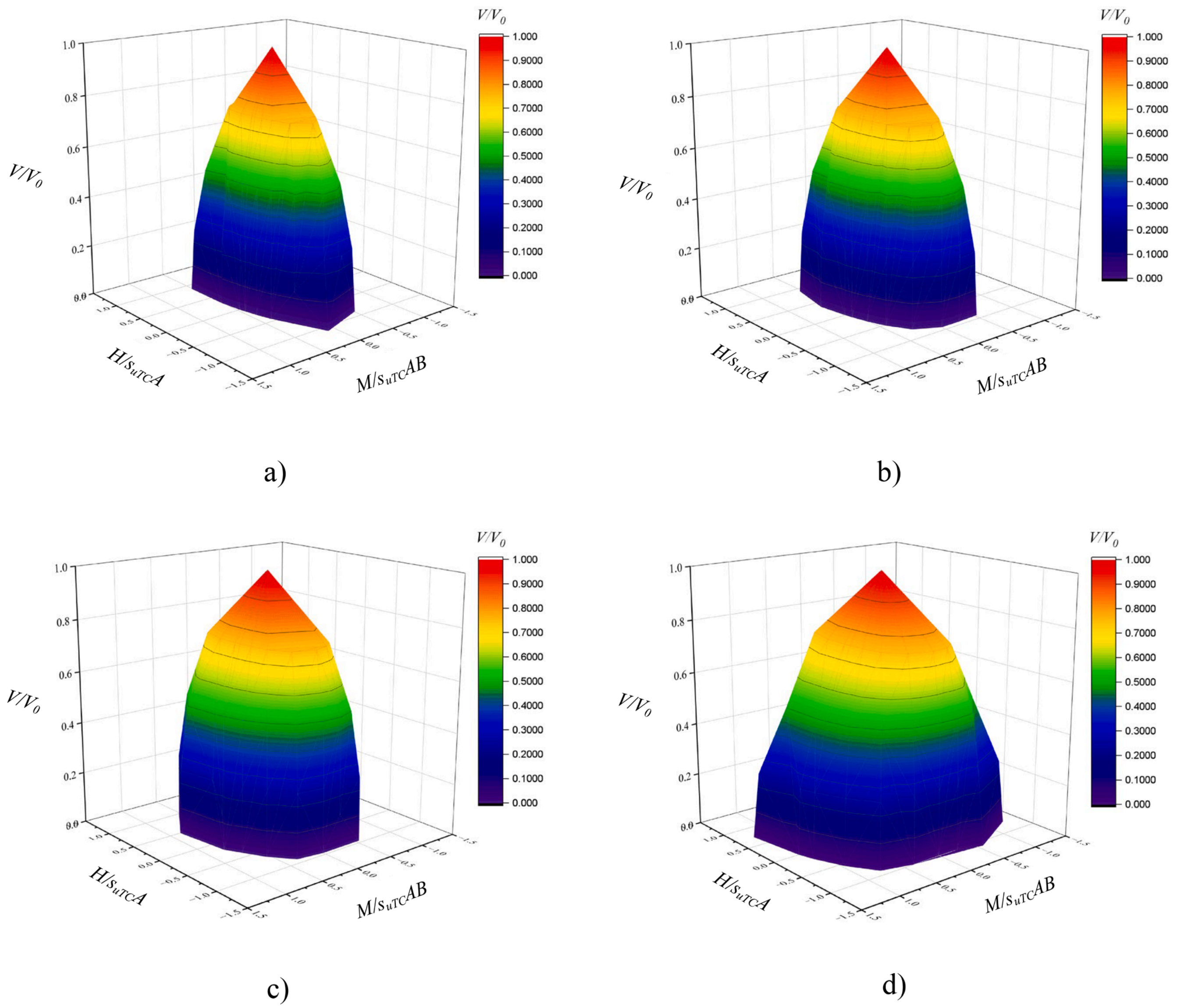

Fig. 17. 3D diagram representation of the combined failure loads for a ring foundation with $r_e = 0.7$ and (a) $r_i/r_o = 0$, (b) $r_i/r_o = 0.2$, (c) $r_i/r_o = 0.4$, (d) $r_i/r_o = 0.6$.

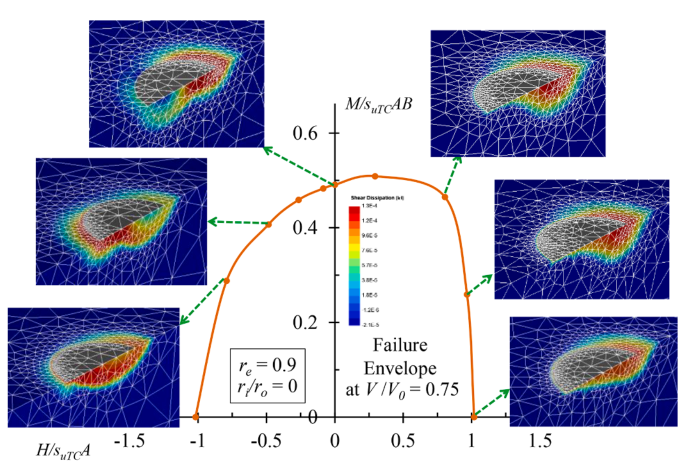

Fig. 18. Failure mechanism of a 2D failure envelope of a ring foundation under general loading for $r_e = 0.9$, $r_i/r_o = 0$, and $V/V_0 = 0.75$.

(2022) by approximately 0.4 % to 5.7 %.

The last verification is shown in Fig. 11(c) for the case of the $H-M$ failure envelope of the ring footing with $r_i/r_o = 0.4$ and $r_e = 1$. The numerical results show some discrepancy between the two solutions, mostly because different mathematical criteria are employed for determining failure. The earlier solutions relied on the Tresca model, whereas this study adopted the AUS model. The difference arises from the use of adaptive elements and plate elements for the ring footing. Specifically, the failure envelope in the $H-M$ planes from the current analysis is approximately 0.7 % smaller in the second and fourth quadrants than in the previous solutions. Although there is an approximately 10 % difference in the estimated capacity in the first and third quadrants due to variations in the failure criteria used, the figure shows that both methods produce similar normalized capacities. Overall, the present FELA solutions align well with those from Birid and Choudhury (2022) across all combinations of *V-H, V-M*, and *H-M* loads.

5. Results and discussion

5.1. FELA results and discussion

The comprehensive solutions for the failure envelope of a ring

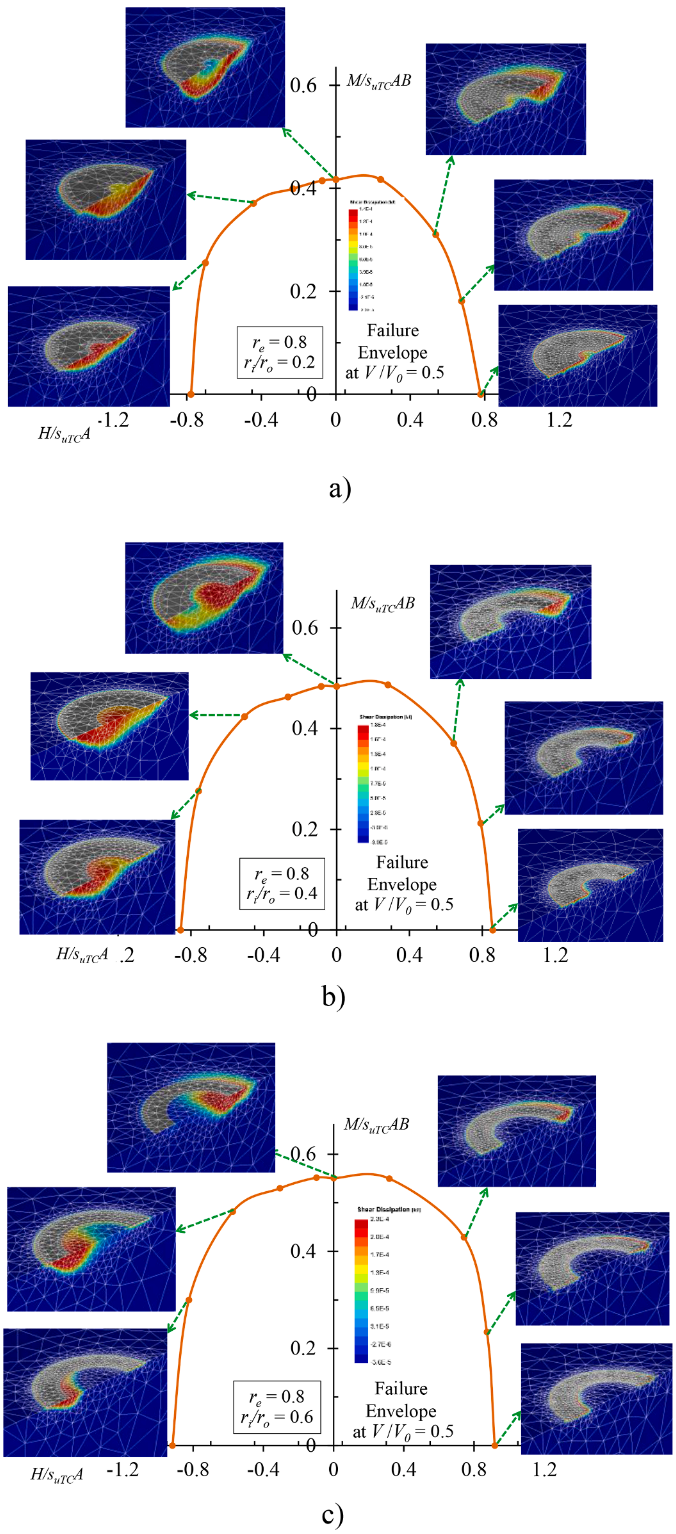

Fig. 19. Failure mechanism of a 2D failure envelope of a ring foundation for $r_e = 0.8$, $V/V_0 = 0.5$ and (a) $r_i/r_o = 0.2$, (b) $r_i/r_o = 0.4$, (c) $r_i/r_o = 0.6$.

foundation on anisotropic clay are presented in Figs. 12, 13, 14, and 15 for *V-H, V-M*, and *H-M* loading spaces, respectively. In Fig. 12, four different ring geometries (r_i/r_o) are investigated to explore the shape and dimensions of the failure envelopes. In addition, the effects of the anisotropic ratios (r_e) are also studied for each ring foundation. For each ring geometry, the numerical results show that the failure envelope expands in the $V-H$ loading space as the value of (r_e) increases from 0.5 to 1.0. Given that $r_e = 1.0$ stands for isotropic soil, the lower the r_e value is, the smaller the failure envelope. Additionally, the maximum value of $V/s_{uTC}A$ decreases from 6.06 to 5.77 as the ring foundation area decreases (i.e., r_i/r_o increases from 0 to 0.6). In contrast, $H/s_{uTC}A$ shows an insignificant rise across all r_i/r_o scenarios because the primary resistance to horizontal loads comes from the shear strength and lateral earth pressure of the soil, which are not significantly influenced by the horizontal area of the foundation.

The numerical results for the $V-M$ loading space are presented in Fig. 13. This study follows the same approach as in Fig. 12, where four different ring geometries (r_i/r_o) are investigated for various (r_e) = 0.5 to 1.0. Notably, both the ratios of $V/s_{uTC}A$ and $M/s_{uTC}AB$ increase as the value of r_e increases for all the ring shapes (r_i/r_o). In addition, the value of $M/s_{uTC}AB$ increases substantially as (r_i/r_o) increases, resulting in an expansion of the failure envelopes.

Fig. 14 shows the variations in the failure envelopes in the $H-M$ loading spaces at $V/V_0 = 0.5$. Similar to Figs. 12 and 13, these variations consider ring geometries (inner to outer radius ratio, r_i/r_o) and anisotropic ratios (r_e). While symmetric failure envelopes are observed for *V-H* and *V-M* loading conditions (Figs. 12 and 13), the *H-M* failure envelopes exhibit an asymmetric trend when subjected to both positive and negative horizontal loads ($H/s_{uTC}A$). Note that the failure envelope tends to increase as the r_i/r_o ratio increases. This is likely due to the reduced surface area of the ring, even though the moment capacity increases with increasing r_i/r_o values. Additionally, note that the moment capacity $M/s_{uTC}AB$ and horizontal capacity $H/s_{uTC}A$ increase with increasing r_e for all ring geometries.

The combined effects of $V-H-M$ forces acting on the ring foundation are further investigated in Fig. 15. This analysis aims to create ($V/s_{uTC}A$)-($H/s_{uTC}A$)-($M/s_{uTC}AB$) failure load contours and thereafter to develop three-dimensional failure surfaces. The 2D and 3D contours for these failure loading combinations on ring foundations with $r_i/r_o = 0.2$, $r_e = 0.5$, 0.7, 0.9, and 1 are shown in Fig. 15(a-d), respectively. Fig. 15 shows the failure surface in the $H-M$ space by merging these envelopes with those affected by the bending moment (*M*) and horizontal load (*H*) at different levels of vertical load as (V/V_0 = 0 to 0.75). Notably, the total area of the failure envelope decreases as the value of (V/V_0) increases. Indeed, as the vertical load level increases, the failure envelope decreases.

Fig. 15 can be further extended to 3D failure contour envelopes, as shown in Figs. 16 and 17. Fig. 16(a-d) illustrates the 3D failure envelope (V/V_0, $H/s_{uTC}A$, $M/s_{uTC}AB$) in the cases where $r_i/r_o = 0.4$ and $r_e = 0.5$, 0.6, 0.8, and 1, respectively. Increasing the value of r_e expands the 3D failure envelope, which assumes the shape of a vertically rotating ellipsoid. The plots for both $r_e = 0.5$, 0.6, 0.8, and 1 show that the size of the contour decreases as V/V_0 increases. The 3D failure surfaces for the cases $r_e = 0.7$ and $r_i/r_o = 0$, 0.2, 0.4, and 0.6 are presented in Fig. 17. The shape and size of the 3D failure envelope expand when the value of r_i/r_o increases. This can be explained by the horizontal and moment capacity in the 2D failure envelope increasing with increasing r_i/r_o, as shown in Fig. 14. This combined representation provides a clear visualization of how the surfaces transform because of the various vertical load levels (V/V_0).

Several demonstrations of the failure patterns (or mechanisms) are shown in Fig. 18 for foundations subjected to various load combinations (*V-H-M*). Shear power dissipations are used for this demonstration purpose ($r_e = 0.9$, $r_i/r_o = 0$, and $V/V_0 = 0.75$). Six cases are examined, corresponding to different values of β angles, including $\beta = 0°$, 15°, 30°, 90°, 140°, and 160°. In the first quadrant, where the (β) angle ranges to 90°, the failure mechanism is similar to a scoop mechanism developed under combined horizontal and moment loading. A pure bending moment failure is observed, where the ultimate moment M_0 is mobilized, whereas a pure horizontal mechanism is developed with the rigid translation of soil occurring in the back and bottom of the ring foundation, and H_0 is mobilized at $\beta = 0°$. Unlike other load combinations in the first quadrant, the induced mechanism does not extend to the ground

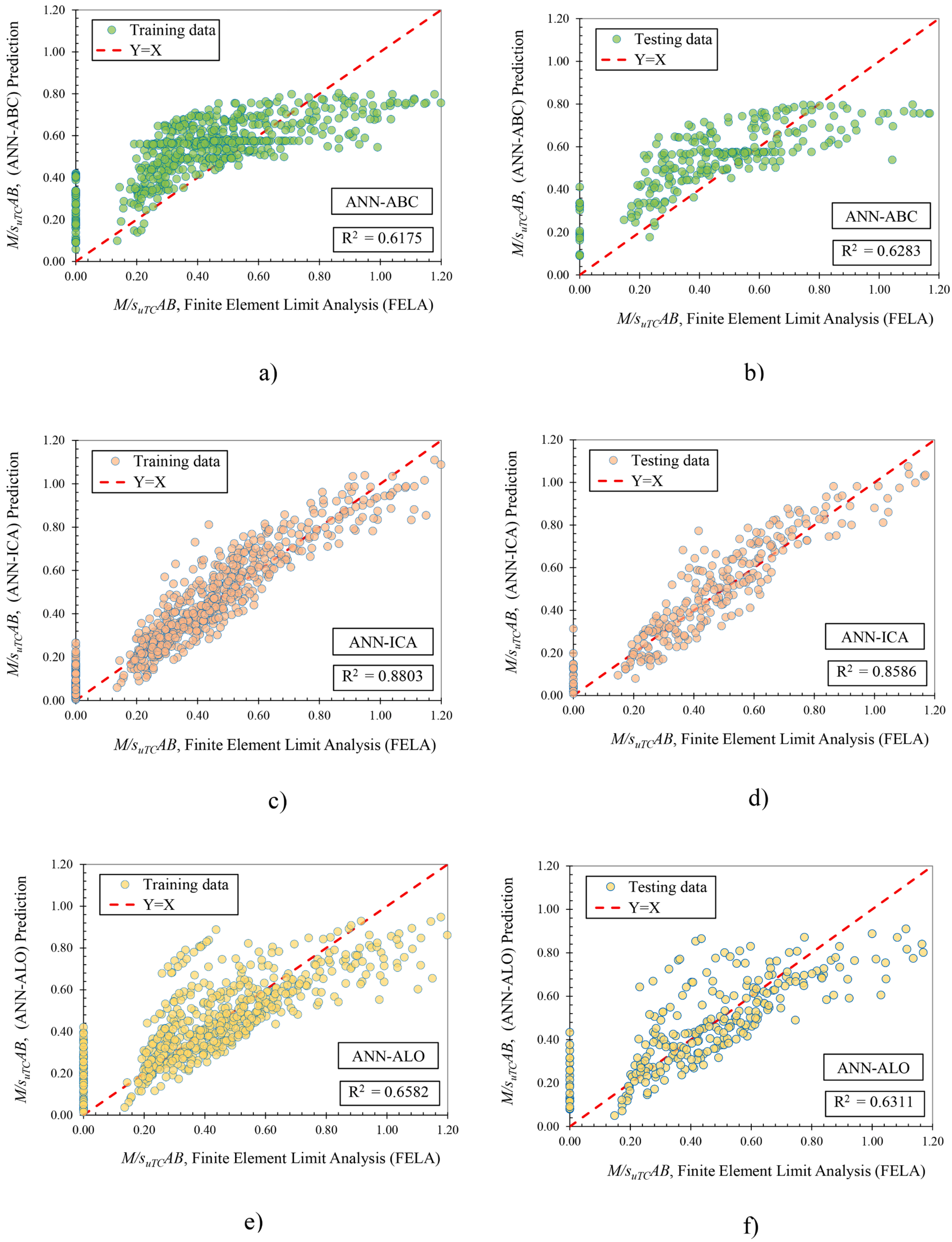

Fig. 20. Comparison of actual FELA results with those from ANN for $M/s_{uTC}AB$ with a) train ANN-ABC, b) test ANN-ABC, c) train ANN-ICA, d) test ANN-ICA, e) train ANN-ALO, f) test ANN-ALO.

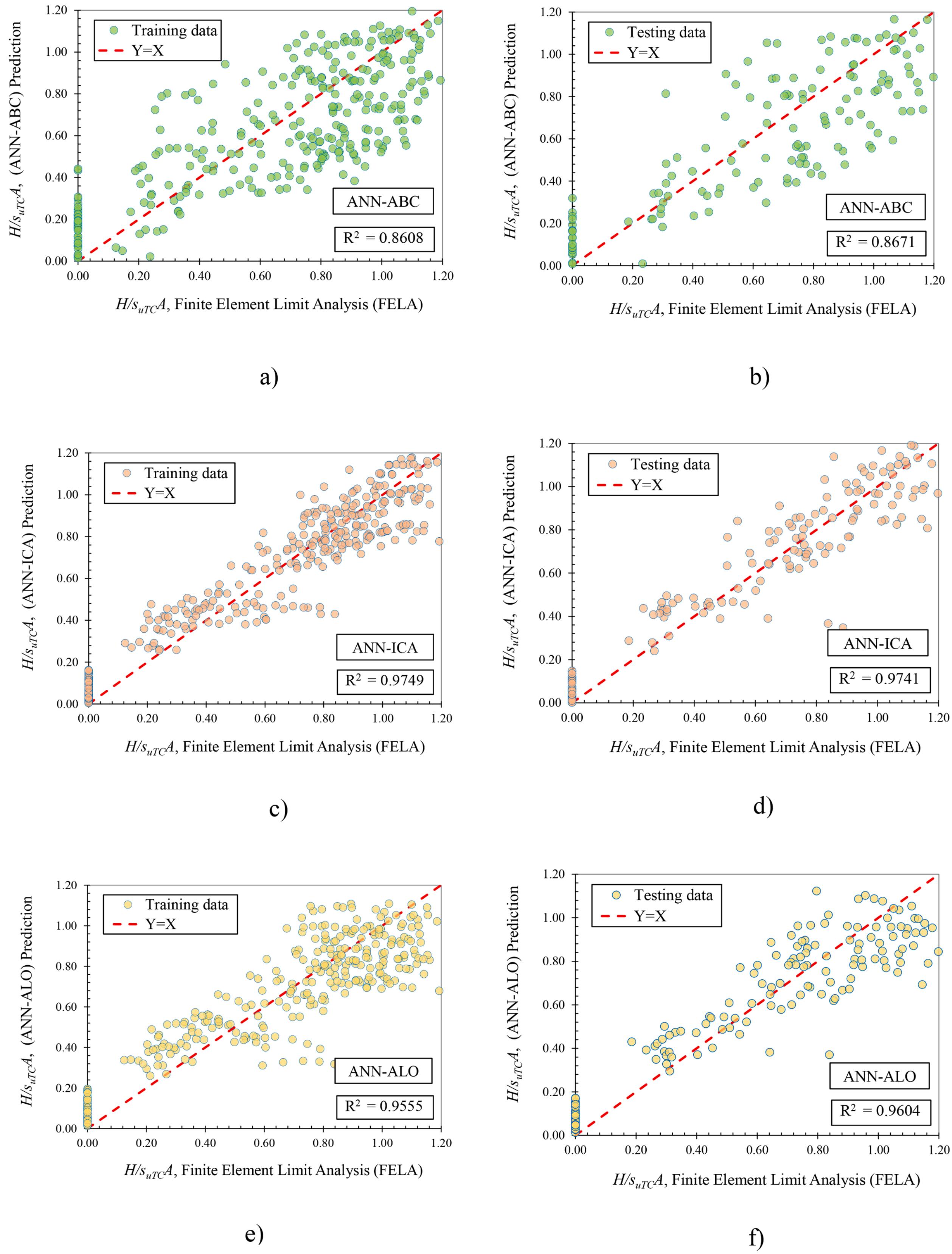

Fig. 21. Comparison of actual FELA results with those from ANN for $H/s_{uTC}A$ with a) train ANN-ABC, b) test ANN-ABC, c) train ANN-ICA, d) test ANN-ICA, e) train ANN-ALO, f) test ANN-ALO.

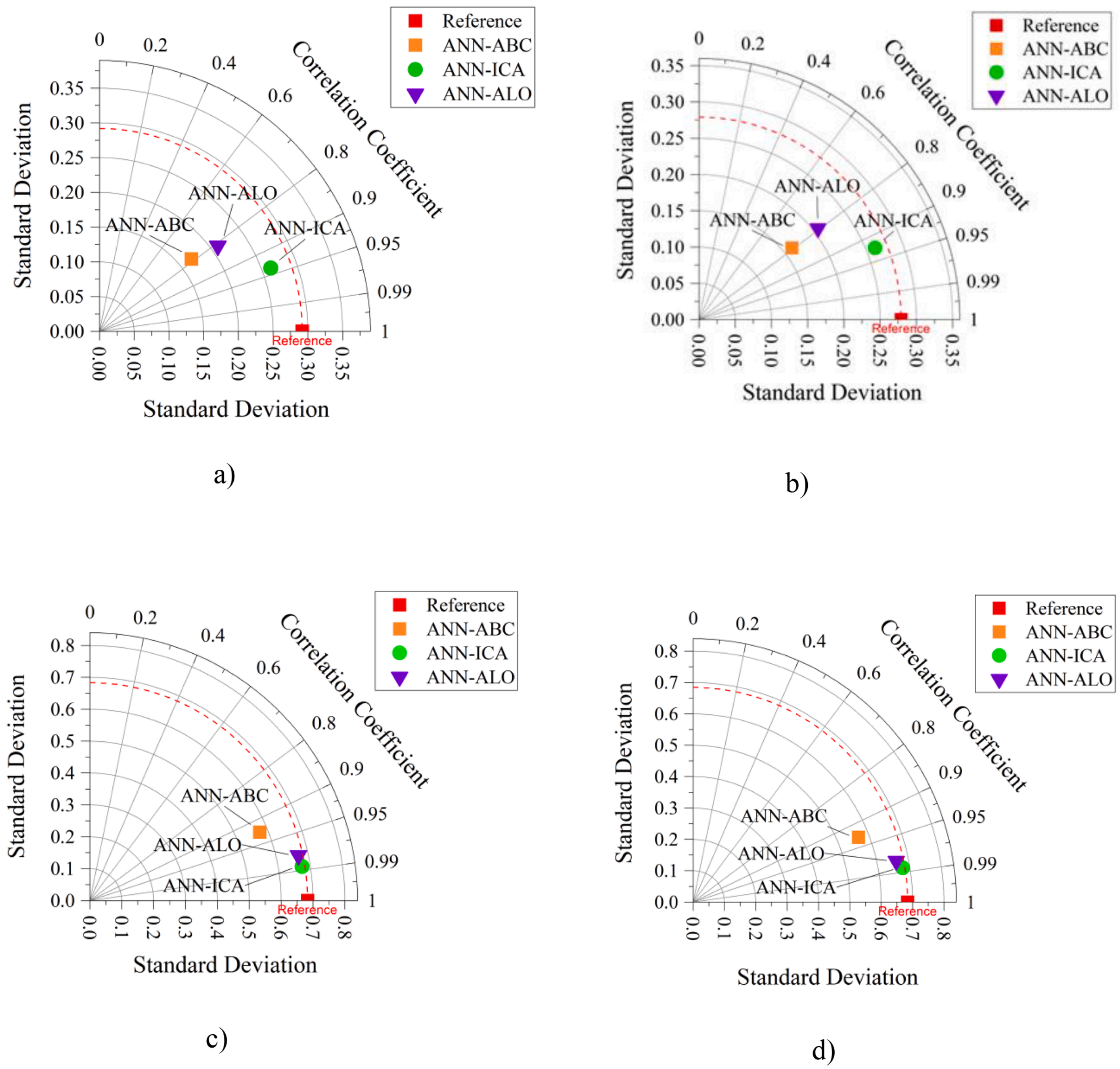

Fig. 22. Taylor diagrams for a) $M/s_{uTC}AB$ training, b) $M/s_{uTC}AB$ testing, c) $H/s_{uTC}A$ training, and d) $H/s_{uTC}A$ testing.

surface at the sides, resulting in a scoop-wedge mechanism because the directions of the horizontal force and bending moment are different.

Fig. 19(a-c) shows a comparison of failure mechanisms under different combinations of horizontal loads and bending moments, specifically for conditions where $r_e = 0.8$, $V/V_0 = 0.5$, and $r_i/r_o = 0.2$, 0.4, and 0.6, respectively. The observed failure mechanisms result from both rotational and translational modes, providing practical insights for practical applications. Each point within the envelope represents the final position where soil displacement ceases during collapse. At $\beta = 0^\circ$, a pure sliding mechanism occurs, where soil rigidly translates at the base of the footing due to interface conditions, and H_0 is activated. As β reaches 90°, the plastic zone expands, resulting in a Brinch Hansen mechanism (see Fig. 6c). When β approaches 180°, the shear plane transforms from Brinch Hansen mechanism to an asymmetric wedge mechanism at the back and bottom of the foundation for all the cases of $r_i/r_o = 0.2$, 0.4, and 0.6 (refer to Fig. 6c and d). Note that these plots are for illustrating purposes, as they are not actual representatives of real applications in conical foundations. For the sake of completeness, they are included in the paper.

5.2. ANN and ANN-hybrid optimal algorithm results

Regression plots that compare the FELA solutions and those predicted values of the dimensionless components $M/s_{uTC}AB$ and $H/s_{uTC}A$ are presented in Figs. 20 and 21 for various machine learning models (i.e., ANN-ABC, ANN-ICA, and ANN-ALO). This comparison is performed for both the training and testing phases. On the basis of the regression plots, it can be concluded that all the models successfully captured the relationships between the input and predictor variables. Among the three models, the predicted values of ANN-ICA, shown as $M/s_{uTC}AB$ and $H/s_{uTC}A$, are more closely aligned with the line of equality, with R^2 =0.8803 and 0.9749, respectively. Although the other models exhibit comparable data fitting, the performances of all the proposed models are considered reasonably similar. In summary, the ANN-ICA model

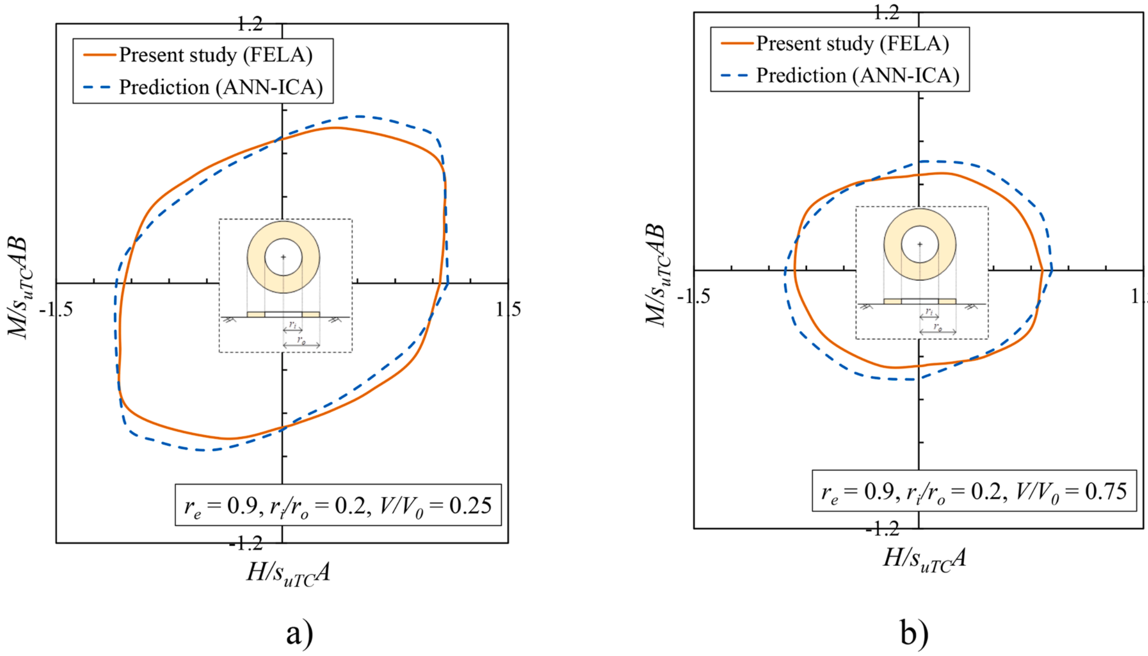

Fig. 23. Comparison of failure envelopes between the present study (FELA) and prediction (ANN-ICA), where $r_e = 0.9$, $r_i/r_o = 0.2$ and a) $V/V_0 = 0.25$, b) $V/V_0 = 0.75$.

performed better than did the ANN-ALO and ANN-ABC models during the training and testing stages. The R^2 values obtained for ANN-ICA were 0.9749 during the training phase and 0.9741 during the testing phase of $H/s_{uTC}A$, as shown in Fig. 21c and d. Similarly, ANN-ALO achieved R^2 values of 0.9555 for training and 0.9604 for testing $H/s_{uTC}A$, whereas ANN-ABC achieved R^2 values of 0.6175 for training and 0.6283 for testing $M/s_{uTC}AB$. Hence, the ANN-ICA model has exceptional performance $H/s_{uTC}A$ and $M/s_{uTC}AB$ in both the training and testing stages, as evidenced by its better R^2 results. It can therefore be concluded that the ANN-ICA model possesses remarkable predictive capacity.

Taylor's diagram is a visual tool introduced by Taylor (2001) to compare various models against a reference dataset. It consolidates multiple statistical metrics, such as the correlation coefficient, root mean square deviation, and standard deviation ratio, thus enabling a quick evaluation of how well datasets match a reference. In this study, Taylor's diagrams for the training and testing phases of $M/s_{uTC}AB$ and $H/s_{uTC}A$ are shown in Fig. 22(a) to (d), respectively, for the three models. In an ideal prediction model, the normalized standard deviation and correlation coefficient are regarded as 1, whereas the root mean square deviation (RMSD) attains a value of 0 (see the red reference point in Fig. 22). Out of the three models in the training phase (orange ANN-ABC, green ANN-ICA, and purple ANN-ALO), the green ANN-ICA model has a normalized standard deviation of 0.7, a correlation coefficient of 0.98, and a root mean square deviation (RMSD) of 0.1 (refer to Fig. 22c). This ANN-ICA model outperforms the other models, is positioned closest to the reference point, and shows superior performance in both the training and testing phases. While the other two models (ANN-ABC and ANN-ALO) cluster slightly farther from ANN-ICA, they still have good potential as a tremendous prediction mode, as the difference in correlation (R^2) among all the models in the training and testing phases is minor. Therefore, it can be concluded that the ANN-ICA model is considered the best performer in this study.

Figs. 23(a-b) compare the predictions of the ANN-ICA model and the FELA technique for the failure envelope of a ring foundation. The comparison is shown at specific values of $r_e = 0.9$, $r_i/r_o = 0.2$, and $V/V_0 = 0.25$ and 0.75. The comparison reveals that the ANN-ICA model's prediction nearly matches the results obtained using the FELA technique, indicating that the proposed model is effective and precise in generating the *V-H-M* failure envelope of ring footings.

6. Conclusion

Failure envelopes of ring footing in anisotropic clay under general loadings (*V-H-M*) have been effectively investigated in this paper using advanced adaptive three-dimensional finite element limit analysis (3D AFELA) and artificial neural networks (ANNs) with optimized ANN models (ANN-ABC, ANN-ICA, and ANN-ALO).

The study began with extensive comparisons between the present solutions and the published results. It then moved on to study the 2D failure envelopes of (*V-H*), (*V-M*), and (*H-M*) on anisotropic clay. The study concluded that the failure envelopes in ring foundations exhibited symmetry under vertical-horizontal (*V-H*) and vertical-moment (*V-M*) planes. Nevertheless, asymmetry was observed in the failure zones under the *H*−*M* planes when all the ring shapes and anisotropy ratios were considered. In general, an increase in the anisotropic ratio (r_e) or the inner and outer dimensions (r_i/r_o) would yield a larger failure envelope. The size of the $H/s_{uTC}A$- $M/s_{uTC}AB$ space at various levels of vertical loading ($V/V_0 = 0$, 0.25, 0.5, 0.75) in the 3D failure envelopes increases by approximately 10 % when r_e changes from 0.5 to 1 and approximately 4.2 %−10.6 % when r_i/r_o changes from 0.6 to 0.

This study also utilized optimized artificial neural network (ANN) models to establish a practical engineering tool for constructing both 2D ($H/s_{uTC}A$, $M/s_{uTC}AB$) and 3D failure envelopes (V/V_0, $H/s_{uTC}A$, $M/s_{uTC}AB$) within the realm of geotechnical research. A comparison of ANN models with different optimization algorithms revealed that ANN-ICA has the greatest efficiency in predicting the 3D failure envelope of ring foundations on anisotropic clay subjected to combined loadings (*V-H-M*) with high accuracy ($R^2 = 97.49$ %). This enhanced ANN model's performance is a highly recommended alternative to assist geotechnical researchers in identifying failure envelopes for ring foundations subject to general *V*−*H*−*M* loadings. Future studies should explore the development of failure envelopes for ring footings in sandy and reinforced soils or integrate more sophisticated soil models that consider torsional loading effects.

6.1. Limitations of the research

The anisotropic properties of the clay might have been modelled via simplified assumptions. This limitation may restrict the accuracy of the failure envelope under more complicated loading conditions or in situations where the anisotropy is highly variable. As a result, the findings might not apply to all types of anisotropic soils, such as those with extreme anisotropy or very soft or stiff clays. The analysis might assume a certain depth or embedment for the ring foundation, which may limit the applicability of the findings. The incorporation of varying depths of embedment foundations could improve the robustness of the findings. This study focused primarily on static loading conditions. In practical offshore or dynamic environments, cyclic or dynamic loading due to wave, wind, or seismic activity is critical, and the failure behavior under these conditions may differ from that in static cases. These limitations suggest several potential avenues for future research: (*i*) expanding the analysis to cover more varied soil conditions, especially different types of anisotropic clays; (*ii*) investigating the impact of cyclic and dynamic loading on the failure envelope; and (*iii*) exploring the effects of foundation embedment depth in greater detail. (*iv*) ANN-ICA was accurate. However, data-dependent machine learning models are common. Optimized hybrid ANN models may not be generalizable to soil conditions or foundation geometries not included in the training data. This constraint may reduce the hybrid ANN tool's practicality in certain geotechnical contexts. The accuracy of the ANN model may be affected by the optimization strategy used, emphasizing the need for more research into its robustness for similar issues. By acknowledging these limitations, the study can position itself for further exploration and refinement in future research.

CRediT authorship contribution statement

Duy Tan Tran: Methodology, Software, Validation, Formal analysis, Visualization, Validation, Writing – original draft. **Jim Shiau:** Conceptualization, Validation, Supervision, Writing – review & editing, Funding acquisition. **Divesh Ranjan Kumar:** Conceptualization, Methodology, Validation, Visualization, Writing – original draft. **Van Qui Lai:** Methodology, Software, Formal analysis, Visualization, Writing – review & editing. **Suraparb Keawsawasvong:** Conceptualization, Methodology, Validation, Formal analysis, Visualization, Writing – original draft.

Declaration of competing interest

The authors declare that they have no known competing financial interests or personal relationships that could have appeared to influence the work reported in this paper.

Acknowledgement

We acknowledge Ho Chi Minh City University of Technology (HCMUT), VNU-HCM for supporting this study.

References

Armaghani, D.J., Momeni, E., Abad, S.V.A.N.K., Khandelwal, M., 2015. Feasibility of ANFIS model for prediction of ground vibrations resulting from quarry blasting. Environ. Earth. Sci. 74, 2845–2860.
Atashpaz-Gargari, E., Lucas, C., 2007. Imperialist competitive algorithm: an algorithm for optimization inspired by imperialistic competition. In: 2007 IEEE Congress on Evolutionary Computation. CEC, pp. 4661–4667, 2007.
Benmebarek, S., Remadna, M.S., Benmebarek, N., Belounar, L., 2012. Numerical evaluation of the bearing capacity factor Nγ of ring footings. Comput. Geotech. 44 (6), 132–138.
Birid, K., Choudhury, D., 2021. Undrained bearing capacity factor NC for ring foundations in cohesive soil. Int. J. Geomech. 21 (2), 06020038.
Birid, K., Choudhury, D., 2022. Failure envelopes for ring foundations resting on Tresca soil under combined loading. J. Geotech. Geoenviron. Eng. 148 (11), 04022088.
Boushehrian, J.H., Hataf, N., 2003. Experimental and numerical investigation of the bearing capacity of model circular and ring footings on reinforced sand. Geotextiles Geomembranes 21, 241–256.
Bransby, M.F., Randolph, M.F., 1998. Combined loading of skirted foundations. Geotechnique 48 (5), 637–655.
Bransby, M.F., Yun, G.J., 2009. The undrained capacity of skirted strip foundations under combined loading. Geotechnique 59 (2), 115–125.
Brinch Hansen, J., 1970. A revised and extended formula for bearing capacity. Danish Geotech. Inst. Bull. 28, 5–11.
Butterfield, R., 1999. Dimensional analysis for geotechnical engineering. Géotechnique 49 (2), 357–366.
Casagrande, A., Carillo, N., 1944. Shear failure of anisotropic soils. Contribut. Soil Mech. (BSCE) 1941–1953, 122–135.
Chanda, D., Nath, U., Saha, R., Haldar, S., 2021. Development of lateral capacity based envelopes of piled raft foundation under combined V-M-H loading. Int. J. Geomech. 21 (6), 0402175.
Chen, H., Shen, Z., Wang, L., Qi, C., Tian, Y., 2022. Prediction of undrained failure envelopes of skirted circular foundations using gradient boosting machine algorithm. Ocean Eng. 258 (6), 111767.
Chen, L., Li, J., Li, Q., Feng, Y., 2021. Strengthening mechanism of studs for embedded-ring foundation of wind turbine tower. Energies. (Basel) 14 (3), 710.
Chen, L., Liu, G., 2018. Upper bound solutions of vertical bearing capacity of skirted mudmat in sand. Appl. Ocean Res. 73 (5), 100–106.
Ciria, H., Peraire, J., Bonet, J., 2008. Mesh adaptive computation of upper and lowerbounds in limit analysis. Int. J. Numer. Methods Eng. 75, 899–944.
DNV, 1992. Classification Notes No. 30. 4. Foundations. Det Norske Veritas.
Du, Y., Qian, S., Fu, X., Chen, H., Li, G., 2022. New model for predicting the bearing capacity of large strip foundations on soil under combined loading. Int. J. Geomech. 22 (5), 04022055.
Dunne, H.P., Martin, C.M., 2017. Capacity of rectangular mudmat foundations on clay under combined loading. Géotechnique 67 (2), 168–180.
El Sawwaf, M., Nazir, A., 2012. Behavior of eccentrically loaded small-scale ring footings resting on reinforced layered soil. J. Geotech. Geoenviron. Eng. 138 (3), 376–384.
Fiumana, N., Bienen, B., Govoni, L., Gourvenec, S., Cassidy, M.J., Gottardi, G., 2019. Combined loading capacity of skirted circular foundations in loose sand. Ocean Eng 183, 57–72.
Gholami, V., Sahour, H., 2022. Simulation of rainfall-runoff process using an artificial neural network (ANN) and field plots data. Theor. Appl. Climatol. 147, 1–12.
Gourvenec, S., 2007. Failure envelopes for offshore shallow foundations under general loading. Geotechnique 57 (9), 715–728.
Gourvenec, S., 2008. Effect of embedment on the undrained capacity of shallow foundations under general loading. Geotechnique 58 (3), 177–185.
Gourvenec, S., Barnett, S., 2011. Undrained failure envelope for skirted foundations under general loading. Géotechnique 61 (3), 263–270.
Gourvenec, S.M., Randolph, M.R., 2003. Effect of strength non-homogeneity on the shape and failure envelopes for combined loading of strip and circular foundations on clay. Géotechnique 53 (6), 575–586.
Hagan, M.T., Menhaj, M.B., 1994. Training feedforward networks with the Marquardt algorithm. IEEE Trans. Neural Netw. 5 (6), 989–993.
Hataf, N., Razavi, M.R., 2003. Model test and finite element analysis of bearing capacity of ring footings on loose sand. Iran J. Sci. Technol. Trans. B. 27 (B1), 47–56.
Jitchaijaroen, W., Wipulanusat, W., Keawsawasvong, S., Chavda, J.T., Ramjan, S., Sunkpho, J., 2023. Stability evaluation of elliptical tunnels in natural clays by integrating FELA and ANN. Results. Eng. 19, 101280.
Karaboga, D., 2005. An Idea Based on Honey Bee Swarm for Numerical Optimization. Department of Computer Engineering, Engineering Faculty, Erciyes University. Technical Report-TR06.
Keawsawasvong, S., Sangjinda, K., Jitchaijaroen, W., Alzabeebee, S., Suksiripattanapong, C., Sukkarak, R., 2023. Soft computing-based models for estimating the ultimate bearing capacity of an annular footing on Hoek–Brown material. Arab. J. Sci. Eng. 1–8.
Keawsawasvong, S., Shiau, J., Ngamkhanong, C., Lai, V.Q., Thongchom, C., 2022. Undrained stability of ring foundations: axisymmetry, anisotropy, and nonhomogeneity. Int. J. Geomech. 22 (1), 04021253.
Keawsawasvong, S., Ukritchon, B., 2016. Three-dimensional interaction diagram for the undrained capacity of inverted T-shape strip footings under general loading. Int. J. Geotech. Eng. 12 (2), 133–146.
Keshavarz, A., Kumar, J., 2017. Bearing capacity computation for a ring foundation using the stress characteristics method. Comput. Geotech. 89 (9), 33–42.
Krabbenhoft, K., Galindo-Torres, S.A., Zhang, X., Krabbenhoft, J., 2019. AUS: anisotropic undrained shear strength model for clays. Int. J. Numer. Anal. Methods Geomech. 43 (17), 2652–2666.
Krabbenhoft, K., Lyamin, A., Krabbenhoft, J., 2015. Optum computational engineering (OptumG3), Available on: www.optumce.com.
Kumar, B., Samui, P., 2008. Application of ANN for predicting pore water pressure response in a shake table test. Int. J. Geotech. Eng. 2, 153–160.
Kumar, D.R., Samui, P., Burman, A., 2022. Prediction of probability of liquefaction using hybrid ANN with optimization techniques. Arab. J. Geosci. 12 (20), 1–21.
Kumar, J., Chakraborty, M., 2015. Bearing capacity factors for ring foundations. J. Geotech. Geoenviron. Eng. 141 (10), 06015007.
Kumar, J., Ghosh, P., 2005. Bearing capacity factor Nγ for ring footings using the method of characteristics. Canad. Geotech. J. 42, 1474–1484.
Kumar, S., Kumar, D.R., Wipulanusat, W., Keawsawasvong, S., 2024. Development of ANN-based metaheuristic models for the study of the durability characteristics of high-volume fly ash self-compacting concrete with silica fume. J. Build. Eng. 94, 109844. https://doi.org/10.1016/j.jobe.2024.109844.

Ladd, C.C., 1991. Stability evaluations during stage construction. J. Geotech. Eng. 117 (4), 540–615.

Le, L.T., Nguyen, H., Dou, J., Zhou, J., 2019. A comparative study of PSO-ANN, GA-ANN, ICA-ANN, and ABC-ANN in estimating the heating load of buildings' energy efficiency for smart city planning. Appl. Sci. 9 (13).

Lee, J.K., Jeong, S., Lee, S., 2016. Undrained bearing capacity factors for ring footings in heterogeneous soil. Comput. Geotech. 75 (5), 103–111.

Liu, M., Yang, M., Wang, H., 2014. Bearing behavior of wide-shallow bucket foundation for offshore wind turbines in drained silty sand. Ocean Eng. 82, 169–179.

Liu, R., Yuan, Y., Fu, D., Sun, G., 2021. Geotechnical capacities of large-diameter cylindric foundations in clay under general loadings. Appl. Ocean Res. 117, 102951.

Lo, K.Y., 1965. Stability of slopes in anisotropic soils. J. Soil Mech. Found. Divis. 31, 85–106.

Mana, D.K.S., Gourvenec, S., Martin, C.M., 2013. Critical skirt spacing for shallow foundations under general loading. J. Geotech. Geoenviron. Eng. 139 (9), 1554–1566.

Marquardt, D.W., 1963. An algorithm for least-squares estimation of nonlinear parameters. J. Soc. Ind. Appl. Math. 11 (2), 431–441.

Mirjalili, S., 2015. The ant lion optimizer. Adv. Eng. Softw. 83, 80–98.

Mirjalili, S., Jangir, P., Saremi, S., 2017. Multi-objective ant lion optimizer: a multi-objective optimization algorithm for solving engineering problems. Appl. Intell. 46, 79–95.

Narasimhulu, N., Kumar, D.V.A., Kumar, M.V., 2020. LWT based ANN with ant lion optimizer for detection and classification of high impedance faults in distribution system. J. Electr. Eng. Technol. 15, 1631–1650.

Nayyeri, S., Hajali, M., Shdid, C.A., 2016. Ring foundation on elastic subgrade: an analytical solution for computer modelling using the Lagrangian multiplier method. Int. J. Numer. Anal. Methods Geomech. 40 (14), 2017–2030.

Nguyen, D.K., Nguyen, T.P., Ngamkhanong, C., Keawsawasvong, S., Lai, V.Q., 2023. Bearing capacity of ring footings in anisotropic clays: FELA and ANN. Neural Comput. Appl. 1–22.

Panomchaivath, S., Jitchaijaroen, W., Banyong, B., Keawsawasvong, S., Sirimontree, S., Jamsawang, P., 2023. Prediction of undrained lateral capacity of free-head rectangular pile in clay using finite element limit analysis and artificial neural network. Engineered Sci. 24, 923.

Payan, M., Fathipour, H., Hosseini, M., Chenari, R.J., Shiau, J., 2022. Lower bound finite element limit analysis of geo-structures with non-associated flow rule. Comput. Geotech. 147 (2), 104803.

Rabi, M., Ferreira, F.P.V., Abarkan, I., Limbachiya, V., Shamass, R., 2023. Prediction of the cross-sectional capacity of cold-formed CHS using numerical modelling and machine learning. Results. Eng. 17, 100902.

Reddy, Y.R., 2017. Applications of artificial intelligence and machine learning in geotechnical engineering. Int. J. Emerg. Technol. Innov. Res. 2349–5162.

Remadna, M.S., Benmebarek, S., Benmebarek, N., 2017. Numerical evaluation of the bearing capacity factor N'c of circular and ring footings. Geomech. Geoeng. 12 (1), 1–13.

Saha, M.C., 1978. Ultimate Bearing Capacity of Ring Footings on Sand. M.Eng. ThesisUP, University of Roorkee, India.

Sangjinda, K., Kumar, D.R., Keawsawasvong, S., Wipulanusat, W., Jamsawang, P., 2024. Novel neural network-based metaheuristic models for the stability prediction of rectangular trapdoors in anisotropic and non-homogeneous clay. Adv. Eng. Softw. 193, 103668.

Salencon, J., Peeker, A., 1995. Ultimate bearing capacity of shallow foundations under inclined and eccentric loads. Part I: purely cohesive soil. Eur. J. Mech. A/Solids. 14 (3), 349–375.

Shiau, J.S., Yu, H.S., 2000. Shakedown analysis of flexible pavements. In: Proc. of the John Booker Memorial Symposium (ed DW Smith & JP Carter), pp. 643–653.

Shiau, J., Sams, A., Al-Asadi, F., Hassan, M.M., 2018. Stability charts for unsupported plane strain tunnel headings in homogeneous undrained clay. Geomate J. 14 (41), 19–26.

Shiau, J., Keawsawasvong, S., 2022. Producing undrained stability factors for various tunnel shapes. Int. J. Geomech. 22 (8), 06022017.

Shiau, J., Keawsawasvong, S., Yodsomjai, W., 2023. Determination of support pressure for the design of square box culverts. Int. J. Geomech. 23 (1), 06022035.

Shen, Z., Feng, X., Gourvenec, S., 2016. Undrained capacity of surface foundations with zero-tension interface under planar V-H-M loading. Comput. Geotech. 73, 47–57.

Sirimontree, S., Keawsawasvong, S., Ngamkhanong, C., Seehavong, S., Sangjinda, K., 2022. Neural network-based prediction model for the stability of unlined elliptical tunnels in cohesivefrictional soils. Buildings 12 (4), 444.

Sloan, S.W., 2013. Geotechnical stability analysis. Géotechnique 263 (7), 531–572.

Taiebat, H.A., Carter, J.P., 2000. Numerical studies of the bearing capacity of shallow foundations on cohesive soil subjected to combined loading. Géotechnique 50 (4), 409–418.

Tan, F.S., 1990. Centrifuge and Theoretical Modelling of Conical Footings on Sand. Cambridge University, UK. PhD thesis.

Taylor, K.E., 2001. Summarizing multiple aspects of model performance in a single diagram. J. Geophys. Res.: Atmos. 106 (D7), 7183–7192.

Tran, D.T., Tran, M.N., Lai, V.Q., Keawsawasvong, S., 2023. Advanced FELA-ANN framework for developing 3D failure envelopes for strip foundations on anisotropic clays. Model. Earth Syst. Environ. 10 (2), 2375–2392.

Ukritchon, B., Keawsawasvong, S., 2020. Undrained lower bound solutions for end bearing capacity of shallow circular piles in non-homogeneous and anisotropic clay. Int. J. Numer. Anal. Methods Geomech. 44 (5), 596–632.

Xiao, Y., Zhao, M., Zhao, H., 2018. Undrained stability of strip footing above voids in two-layered clays by finite element limit analysis. Comput. Geotech. 97, 124–133.

Yodsomjai, W., Keawsawasvong, S., Lai, V.Q., 2021a. Limit analysis solutions for bearing capacity of ring foundations on rocks using Hoek–Brown failure criterion. Int. J. Geosynth. Ground. Eng. 7 (2), 29.

Yodsomjai, W., Keawsawasvong, S., Senjuntichai, T., 2021b. Undrained stability of unsupported conical slopes in anisotropic clays based on AUS failure criterion. Transp. Infrastruct. Geotechnol. 8 (3).

Yu, L., Yang, Q., Zhang, J., 2018. Undrained bearing capacity of irregular T-bar by the lower bound method in clay. Appl. Ocean Res. 105 (12), 102409.

Zhang, R., Zhao, H., Wu, G., 2022. FELA investigation of eccentrically-loaded footing on parallel tunnels constructed in rock masses. Comput. Geotech. 153, 105102.

Zhao, L., Wang, J.H., 2008. Vertical bearing capacity for ring footings. Comput. Geotech. 35, 292–304.

Zhao, Zihao, Zhang, Hao, Ke, Lijun, Zhao, Guoqing, Meng, Suyun, Wu, Fengyuan, Shiau, Jim, 2022. Effect of loading eccentricity on the ultimate lateral resistance of twin-piles in clay. Soils Found. 62 (2), 1–14. https://doi.org/10.1016/j.sandf.2022.101126.

Zhao, Z., Zhang, H., Shiau, J., Du, W., Ke, L., Wu, F., Bao, X., 2024. Failure envelopes of rigid tripod pile foundation under combined vertical-horizontal-moment loadings in clay. Appl. Ocean Res. 150, 104131.

Zhuang, J., Yin, Z., Kotronis, P., Li, Z., 2019. Advanced numerical modelling of caisson foundations in sand to investigate the failure envelope in the H-M-V space. Ocean Eng 190, 106394.